

Hybrid quantum network for sensing in the acoustic frequency range

Valeriy Novikov,^{1,2,*} Jun Jia,^{1,*} Túlio Brito Brasil,^{1,*} Andrea Grimaldi,^{1,*} Maimouna Bocoum,^{3,1} Mikhail Balabas,¹ Jörg Helge Müller,¹ Emil Zeuthen,¹ and Eugene Simon Polzik¹

¹*Niels Bohr Institute, University of Copenhagen,
Blegdamsvej 17, DK-2100 Copenhagen Ø, Denmark*

²*Russian Quantum Center, Skolkovo, Moscow, Russia*

³*ESPCI Paris, PSL University, CNRS, Institut Langevin, Paris 75005, France*

Ultimate limits for sensing of fields and forces are set by the quantum noise of a sensor. Entanglement allows for suppression of such noise and for achieving sensitivity beyond standard quantum limits. Applicability of quantum optical sensing is often restricted by fixed wavelengths of available photonic quantum sources. Another ubiquitous limitation is associated with challenges of achieving quantum-noise-limited sensitivity in the acoustic noise frequency range relevant for a number of applications. Here we demonstrate a novel tool for broadband quantum sensing by quantum state processing that can be applied to a wide range of the optical spectrum, and by suppressing quantum noise over an octave in the acoustic frequency range. An atomic spin ensemble in the quantum regime is strongly coupled to one of the tunable frequency modes of an Einstein-Podolsky-Rosen (EPR) source of light. The other EPR mode of light, entangled with the first one, is tuned to a disparate wavelength. Engineering the spin ensemble to act as a negative- or positive-mass oscillator we demonstrate frequency-dependent, entanglement-enabled quantum noise reduction for measurements at the disparate wavelength. The tunability of the spin ensemble allows to target quantum noise in a variety of systems with dynamics ranging from kHz to MHz. As an example of the broadband quantum noise reduction in the acoustic frequency range, we analyse the applicability of our approach to state-of-the-art gravitational wave detectors. Other possible applications include continuous-variable quantum repeaters and distributed quantum sensing.

Measurements on mechanical objects, spanning masses from pg to kg, and collective atomic systems, from ultracold atoms to room-temperature ensembles, have reached regimes dominated by quantum dynamics [1–7]. These systems are probed by light at optical or microwave wavelengths where the quantum-coherent interaction surpasses the thermal decoherence. The measurement imprecision due to the quantum fluctuations of light, and the measurement-driven disturbances known as the quantum backaction (QBA) collectively define the minimum total measurement noise called the Standard Quantum Limit (SQL). This constraint sets the limit on sensitivity of quantum sensors of motion [8–11], and restricts applications ranging from biomedical sciences [12] to the exploration of physics beyond the standard model [13].

Unlike a standard optomechanical oscillator [14], an atomic spin oscillator can straightforwardly be engineered to exhibit an effective negative mass [15]. Theoretical proposals for measurements surpassing the SQL using an effective negative mass to counterbalance the quantum backaction of a standard oscillator have been put forward [16–18]. Quantum backaction evasion by coupling a spin oscillator to a macroscopic mechanical oscillator [19, 20] and multi-tone readout of two micromechanical oscillators [21], enabling entanglement of the two systems, have been experimentally demonstrated. However, in those experiments both systems had to interact with light at a specific wavelength defined by the atomic transition. Another limitation of those initial demonstrations was the requirement for the oscillators' frequencies to be in the MHz range whereas the quantum noise re-

duction was achieved within a bandwidth much smaller than that frequency.

Here, we report a hybrid quantum network for the broadband suppression of quantum noise beyond the SQL in the acoustic frequency range with a bandwidth of noise reduction that is comparable to the oscillation frequency. Our protocol, based on connecting a spin oscillator to a sensor through an Einstein-Podolsky-Rosen (EPR) channel, can, in principle, achieve complete quantum noise cancellation [22, 23], while the sensing wavelength can be chosen across a broad range of the optical spectrum. These features make the present approach useful in a number of applications where flexibility of the probe light wavelength and the sensor's eigenfrequency is required.

The main elements of the proposed quantum network are presented in Fig. 1(a). We consider a sensor measuring a force and probed by light at wavelength λ_s , while an atomic oscillator with tunable dynamics interacts with light at wavelength λ_i . The light phase quadrature after passing through the sensor is $P_s = p_s + \mathcal{K}_s x_s + f$, where f is the force signal, (p_s, x_s) , (P_s, X_s) are input/output light canonical variables obeying $[x_s, p_s] = i$. In addition to the imprecision noise $\propto p_s$, the interaction induces the quantum backaction $\propto x_s$, which scales with the *frequency-dependent* coupling strength $\mathcal{K}_s(\Omega)$. Similarly, after interaction with the atomic spin ensemble, the light phase quadrature reads $P_i = p_i + \mathcal{K}_a(\Omega)x_i$. We demonstrate that we can engineer the spin oscillator to provide a counter-response of the sensor $\mathcal{K}_a(\Omega) = -\mathcal{K}_s(\Omega)$ corresponding to a negative-mass oscillator. The ideal EPR state of light between signal and idler wavelengths λ_s

and λ_i introduces correlations such that the uncertainties $\Delta(p_i + p_s) \rightarrow 0$ and $\Delta(x_i - x_s) \rightarrow 0$. Thus, combining the negative-mass response with EPR light it is possible to suppress both the quantum imprecision and backaction noise, $\Delta(P_s + P_i) = \Delta(p_s + p_i) + \mathcal{K}_s \Delta(x_s - x_i) + f \rightarrow f$, leading to broadband sensitivity gain.

HYBRID QUANTUM NETWORK

The experimental implementation, depicted in Fig. 1(b), involves generating an EPR state of two optical fields: an idler at 852 nm and a signal at 1064 nm. The idler passes through the spin oscillator prepared in an effective-negative-mass configuration. After the spins-idler interaction, we measure the quantum states of light in both the idler and signal arms. We demonstrate that the joint detection results in frequency-dependent conditional squeezing in the signal mode. The optimal conditional squeezing is obtained at the read-out phase angle $\Phi(\Omega)$ determined by the quantum dynamics of the spin oscillator, characterised by $\mathcal{K}_a(\Omega)$. This conditioning is equivalent to the preparation of the squeezed state that compensates for the rotation of the signal output state induced by the target sensor's quantum backaction $\mathcal{K}_s(\Omega)$, thus maintaining noise reduction across all frequencies.

While the approach we present is broadly applicable, we highlight its potential by examining quantum enhancements in Gravitational Wave Detectors (GWDs) [22]. Current GWDs are now operating near the SQL [3, 4] and rely on frequency-dependent squeezing to broaden their observational range [24, 25], and demonstrate squeezing of the quantum noise in the interferometer [26]. This technique [27], which employs a 300-meter filter cavity to rotate the squeezed state, is effective, but challenging to scale, particularly for the anticipated detuned dual-recycling Fabry-Pérot Michelson interferometer design of the next GWD generation [28]. In this configuration, the detector susceptibility will require an additional hundred-meter-long filter cavity [11]. Different approaches are currently under investigation [29–31], but they are strongly limited by interdependencies with interferometer design [32]. In this context, we propose a new method for generating frequency-dependent squeezing that achieves performance comparable to the filter cavity approach while offering a more compact and flexible setup.

ATOM-LIGHT TWO-COLOUR QUANTUM CHANNEL

Our EPR source design, based on a Nondegenerate Optical Parametric Oscillator (NOPO), enables the frequency-tunable entangled modes to couple to a specific

target system (see Methods). Here we choose the signal at $\lambda_s = 1064$ nm compatible with contemporary GWDs and the idler at $\lambda_i = 852$ nm tuned to the ^{133}Cs D₂ line. Due to the parametric amplification, the signal and idler will individually display a noise level higher than that of vacuum fluctuations (shot noise). EPR correlations allow the measurement on one mode to be used to infer the measurement outcome of another mode with precision below the vacuum fluctuations, which results in *conditional squeezing* [33]. For a given optical mode k , the x_k (amplitude) and p_k (phase) quadratures define a general detection quadrature $q_k(\theta_k) = x_k \sin \theta_k + p_k \cos \theta_k$, selected by the homodyne angle θ_k . We consider the case of measurements on the idler mode used to estimate the outcome of measurements on the signal mode. In this case, the signal mode is conditionally squeezed if the inferred variance obeys $\text{Var}[q_s(\theta_s) + gq_i(\theta_i)] < 1/2$, thus manifesting the reduction of the noise compared to the vacuum level 1/2. The gain factor g is selected to minimize the variance. In the output of the NOPO, correlations are maximized by the choice of quadratures satisfying the condition for detection angles $\theta_i = -\theta_s$ [33], where the phases are referenced to the pump beam phase (see Methods). For the signal and idler on resonance and the noise sideband frequency well within the NOPO cavity bandwidth, the conditional squeezing is *frequency independent*. The gray trace in the top panel of Fig. 2 shows 3 dB of signal squeezing conditioned on the idler. For comparison with other experiments, we point out that we also measured 6 dB of entanglement of EPR state according to the Duan-Simon criterion as shown in Extended Data Fig. 2(a).

Using optical pumping, we prepare the atomic ensemble in a highly polarized state, with the orientation of the collective atomic spin aligned along the bias field. The idler entangled mode is overlapped with orthogonally polarized strong probe laser beam, which also serves as the Local Oscillator (LO_i) see Fig. 1(b). Both beams are detuned by 1.6 GHz from the transition $6^2\text{S}_{1/2}, F = 4 \leftrightarrow 6^2\text{P}_{3/2}, F' = 5$. The detuning provides sufficient quantum dispersive coupling to the atomic ensemble while significantly reducing the deleterious absorption.

After interacting with the atomic ensemble, the quantum state in the idler mode is measured with a polarimetric homodyne detector. The detection setup comprises a Quarter-Wave Plate (QWP) that introduces a phase offset $\delta\theta_i$ in the idler mode [Fig. 1(b)]. This phase shift contributes to the detection phase θ_i and enables the observation of the ponderomotive squeezing induced by the atomic spin ensemble [34]. The signal mode undergoes free propagation to the second homodyne detector, with the detected quadrature controlled by the relative LO_s phase θ_s . The photocurrents corresponding to each homodyne detector are recorded for postprocessing. A detailed description of the experimental setup is given in the Methods.

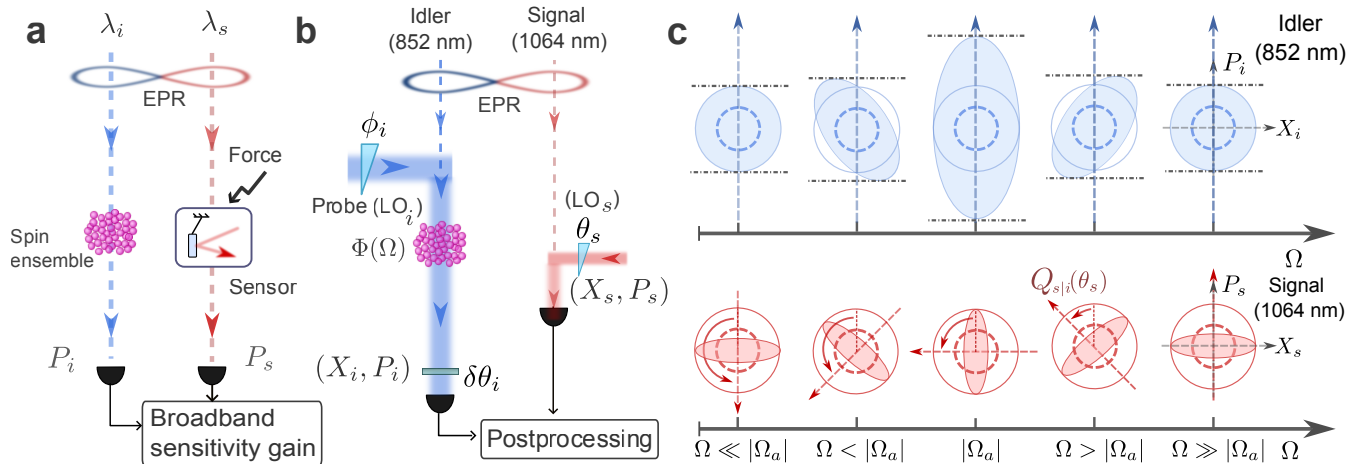


Figure 1. **Parallel approach to broadband quantum noise suppression.** (a) General parallel scheme for the sensitivity enhancement of a quantum-noise-limited sensor. (b) Layout of the experimental setup. The spin ensemble is probed by light at 852 nm (idler) which is entangled with a 1064 nm (signal) optical mode. A suitably engineered atomic spin ensemble provides the required quadrature-rotation dynamics, described by $\Phi(\Omega)$. The two modes are analysed by the corresponding homodyne detectors with θ_s defining the phase of the signal mode, and the phases ϕ_i and $\delta\theta_i$ defining the detection phase θ_i for the idler mode. Conditioning the signal photocurrent on the idler which has interacted with the spin ensemble results in the noise reduction spectrum required for a particular application. (c) The noise in the phase space for the idler (blue) and the signal (red) modes as a function of the frequency Ω . Far away from Ω_a the idler noise (blue shaded area) corresponds to the EPR state. Closer to Ω_a the idler experiences a single axis twisting transformation due to interaction with the atomic spin ensemble. Conditioning the signal on the idler by the post-processing of the photocurrents, as shown in panel b, results in squeezing of the signal in the observable $Q_{s|i}(\theta_s)$ where the squeezing phase $\theta_s = \Phi(\Omega)$, as illustrated by the rotated red shaded ellipses in the lower panel. This process counteracts the quantum noise induced by optical probing of the force sensor, thus enabling broadband quantum-enhanced sensing. Dashed circles indicate vacuum noise.

TUNABLE FREQUENCY-DEPENDENT CONDITIONAL SQUEEZING

The atomic spin ensemble affects the phase quadrature of the idler beam in a frequency-dependent way

$$P_i(\Omega) = p_i(\Omega) + \mathcal{K}_a(\Omega)x_i(\Omega) + N_a(\Omega), \quad (1)$$

while leaving the amplitude quadrature unchanged $X_i(\Omega) = x_i(\Omega)$ [19]. $P_i(\Omega)$ contains contributions from both the input phase quadrature p_i and the QBA which is proportional to x_i . This transformation is called one-axis twisting [35, 36]. To achieve a broadband quantum noise reduction the one-axis twisting should be made frequency dependent. Such frequency dependence is delivered by the atoms as illustrated in Fig. 1(c). Its frequency dependence is expressed by

$$\mathcal{K}_a(\Omega) = \frac{\Gamma_a \Omega_a}{\Omega_a^2 + (\gamma_a/2)^2 - \Omega^2 - i\gamma_a \Omega}, \quad (2)$$

where Γ_a is the atomic readout rate, γ_a is the spin decay rate, and Ω_a is the Larmor frequency; $N_a(\Omega)$ represents the atomic noise associated with the finite decay $\gamma_a > 0$, contaminating the output state of light [Eq. (1)]. The sign of Ω_a is determined by that of the effective oscillator mass, and can be switched from positive to negative by adjusting the bias field direction relative to the collec-

tive spin orientation, while varying the bias field strength tunes $|\Omega_a|$ [15, 19].

Efficient broadband quantum noise reduction in our scheme requires strong light-spins coupling, which is characterized by high quantum cooperativity $C_q = \Gamma_a / [\gamma_a(1 + 2n_{\text{th}})]$ [20], where n_{th} is the thermal occupation. We characterize the cooperativity by observing ponderomotive squeezing generated by the spin oscillator ranging from 1 MHz down to 3 kHz [34] (see Methods and Extended Data Fig. 2b).

The effect of the spin oscillator on the quantum state of the idler light [Eq. (1)] is, in our experiments, effectively a frequency-dependent rotation of the input quadratures determined solely by $\mathcal{K}_a(\Omega)$ [Eq. (2)].

We illustrate this for our experimental regime of slow spin decay $\gamma_a^2 \ll \Omega_a^2, \Gamma_a^2$, in which it is permissible to let $\gamma_a \rightarrow 0$ in Eq. (2); this yields a real \mathcal{K}_a factor, equivalent to a purely in-phase atomic response (see Methods for details). Focusing on the quantum noise contribution of light in Eq. (1), we rewrite it as $P_i(\Omega) = z(\Omega)[p_i(\Omega) \cos \Phi(\Omega) - x_i(\Omega) \sin \Phi(\Omega)]$, thereby separating the atomic processing of light into a quadrature rotation

$$\Phi(\Omega) = -\arctan\{\mathcal{K}_a(\Omega)\}, \quad (3)$$

and an overall amplification factor $z(\Omega) = \sqrt{1 + \mathcal{K}_a^2(\Omega)}$. By conditioning the signal mode detection on measure-

ments of P_i ,

$$Q_{s|i}(\theta_s, \Omega) = q_s(\theta_s, \Omega) + g(\Omega)P_i(\Omega), \quad (4)$$

recorded while probing the atomic ensemble with the entangled idler mode and combined according to a suitably optimized gain $g(\Omega)$, one obtains *conditional squeezing* of the idler beam with *frequency-dependent* squeezing angle $\Phi(\Omega)$. This is witnessed in our setup [Fig. 1(b)] by adjusting the signal detection phase $\theta_s = \Phi(\Omega)$ for each frequency component Ω in order to confirm that this optimally compensates for the conditional rotation induced by the idler [Fig. 1(c)].

The range of the phase shift θ_s spans from 0° to 180° as the Fourier frequency is scanned from $\Omega \gg |\Omega_a| + \Gamma_a$ to $\Omega \ll |\Omega_a| - \Gamma_a$, crossing $\theta_s = 90^\circ$ at the Larmor frequency $\Omega = |\Omega_a|$. Thus, the squeezing ellipse undergoes complete rotation over the frequency range with the bandwidth $2\Gamma_a$. The atomic noise $N_a(\Omega)$ in Eq. (1) does not influence the squeezing angle $\Phi(\Omega)$, but merely degrades the degree of conditional squeezing (see Methods).

The dependence of the rotation on the frequency can be changed by modification of the Larmor frequency Ω_a and spin readout rate Γ_a . Reversing the sign of the effective mass changes the sign of Ω_a in \mathcal{K}_a [Eq. (2)] and consequently, the direction of the frequency-dependent rotation $\Phi(\Omega)$ of the squeezing [Eq. (3)]. Specifically, the effective negative mass of the spin oscillator opens up the opportunity to counterbalance the quantum back-action from radiation pressure in quantum optomechanics. In the limit $|\Omega_a|$, $\gamma_a \ll \Omega$, the phase $\Phi(\Omega) = -\arctan(\Gamma_a \Omega_a / \Omega^2)$ mimics the optomechanical interaction with a free-mass object [11]. The conditional squeezed state thus becomes compatible with GWDs in a simple Michelson configuration and potentially allows for broadband quantum noise reduction in such an interferometer.

QUANTUM NOISE SUPPRESSION IN THE ACOUSTIC FREQUENCY BAND

The optimal gain $g(\Omega)$ is applied for each θ_s to maximise the noise suppression based on the entire idler measurement record (see Methods). The noise reduction below the signal beam shot noise level in a broad frequency range confirms that the atomic ensemble imposes the phase shift on the conditional squeezing angle ranging from $\theta_s = 0^\circ$ to $\theta_s \approx 180^\circ$. As shown in the Figure, the theoretical noise spectra calculated based on independent calibrations as described in the Methods, coincide well with the experimental data. The quantum noise suppression does not reach the level set by the initial entangled state of light due to the broadband spin noise (see Methods) at higher Fourier frequencies and due to the atomic thermal noise near Ω_a .

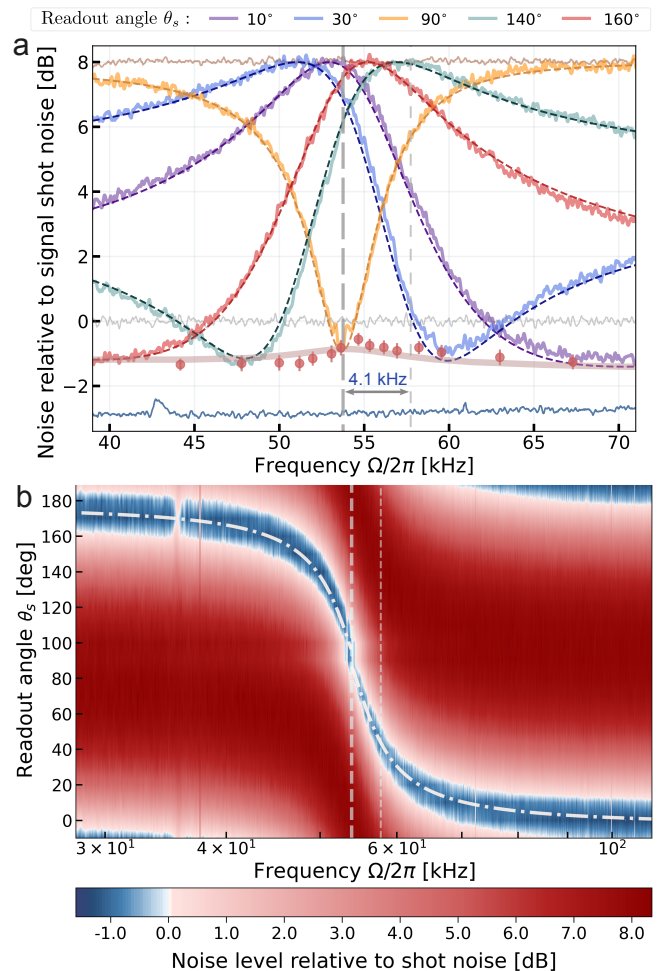


Figure 2. Experimental demonstration and theoretical fit of frequency-dependent conditional squeezing. The spin ensemble is set to the positive-mass configuration with $\Omega_a/2\pi = 54$ kHz (marked by the dashed vertical line), and the idler mode is detected at phase quadrature $\theta_i = 0^\circ$. **(a)** Conditional noise relative to the signal shot noise for different readout angles θ_s . The blue and grey traces represent frequency-independent conditional squeezing and signal mode shot noise, respectively, measured by setting the Larmor frequency to 1 MHz. For each measurements phase, the dark dashed curves represent the fit with our theoretical model. The red data points with error bars are extracted from 60 samples around the minimal noise for each phase. The red solid curve is the conditional squeezing predicted by the model. **(b)** Contour spectrogram of the recorded conditional squeezing, illustrating its dependence on frequency $\Phi(\Omega)$, indicated by the white dashed curve. The bandwidth $\delta\Omega_{\text{SQL}}/2\pi \approx 4.1$ kHz over which the squeezing phase rotates from 90° to 45° is indicated in both panels (see comments in the text).

Following the approach used in spectra Fig. 2(a), a total of 18 conditional squeezing measurements are combined to construct a contour spectrogram, where the conditional noise is presented as a function of both signal homodyne phase θ_s and Fourier frequency Ω . The result in Fig. 2(b) shows the mapping of the frequency-dependent

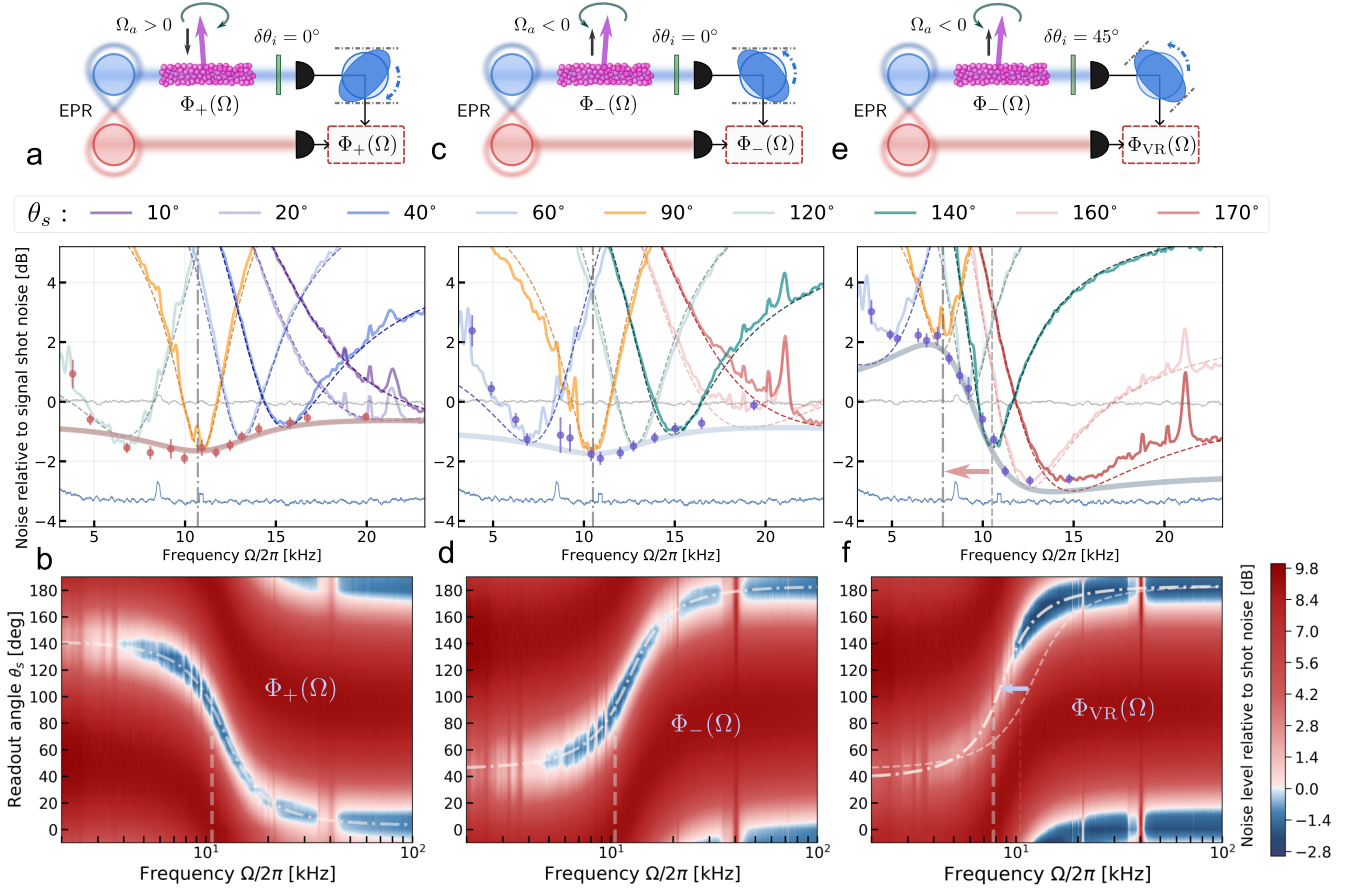


Figure 3. Frequency-dependent conditional squeezing at acoustic frequencies. The inferred quantum noise for the signal mode in three spin ensemble configurations in units of the signal mode shot noise. Top plots (a,c,e) show inferred noise as a function of Fourier frequency, recorded at different readout angles θ_s for specific ensemble configurations. In each plot, the data points represent the measured minimal conditional noise for each readout angle, and the associated thick solid curve shows the prediction from our model. The grey line displays frequency-independent conditional squeezing, measured by detuning the Larmor frequency up to 1 MHz. By combining the data from the joint measurements over the continuous phase range (0° to 180°), we construct the bottom contour spectrograms. **(a, b) Positive mass:** The frequency dependence of squeezing angle $\Phi_+(\Omega)$ with $\Omega_a/2\pi = 10.7$ kHz and the phase offset $\delta\theta_i = 0^\circ$ adjusted by quarter-wave plate in the idler optical mode. **(c, d) Negative mass:** $\Omega_a/2\pi = -10.5$ kHz and $\delta\theta_i = 0^\circ$, showing opposite frequency-dependence $\Phi_-(\Omega)$ to the positive mass. **(e, f) Negative mass with virtual frequency shift:** for the same ensemble parameters as in (c, d), the phase offset is set to $\delta\theta_i \approx 45^\circ$. The gray dash-dotted vertical line, representing the frequency corresponding to the minimum quantum noise for the signal phase of $\theta_s = 90^\circ$ in (e), indicates an effective frequency downshift of ≈ 2.7 kHz (as shown by red arrow) relative to the Larmor frequency, marked by the dashed line. In (f), this frequency downshift also sharpens the frequency-dependent phase rotation [as indicated by the dashed-dotted curve $\Phi_{VR}(\Omega)$ relative to the dashed curve $\Phi_-(\Omega)$]. Meanwhile, we observe enhanced squeezing levels above the Larmor frequency $|\Omega_a|$ compared to (c,d). The total detection phase $\theta_i = 0^\circ$ was chosen for each of three configurations outlined above.

rotation $\Phi_+(\Omega)$. The observed trajectory matches well with the theoretical model (white dashed curve) based on the calibrated experimental values of Γ_a , γ_a and Ω_a (see Methods). The model predicts that in the limit of $|\Omega_a| \gg \Gamma_a, \gamma_a$, the bandwidth $\delta\Omega_{SQL} > 0$ over which the squeezing phase rotates from the amplitude quadrature [$\Phi(\Omega_a) = 90^\circ$] to halfway between amplitude and phase quadratures [$\Phi(\Omega_a + \delta\Omega_{SQL}) = 90^\circ \mp \text{sign}(\Omega_a)45^\circ$] is $\delta\Omega_{SQL}/2\pi \approx \Gamma_a/4\pi = 4.1$ kHz. As shown in Fig. 2(a), this value aligns well with the experimentally observed frequency difference between the Larmor frequency and

the Fourier frequency, at which the squeezing ellipse is rotated by 45° .

After validating the model, we test the system's tunability by lowering the oscillator frequency into the audio band, $|\Omega_a|/2\pi \approx 10$ kHz. We optimised the system, increasing the stability of the EPR source and its coupling to the atomic spin oscillator. The results are shown in Fig. 3. For the positive-mass configuration (a,b), we confirm the broadband conditional squeezing capabilities of our system by measuring the bandwidth of the phase shift $\delta\Omega_{SQL}/2\pi \approx 4.1$ kHz comparable to the central fre-

quency $|\Omega_a|$ and in agreement with the theoretical model (see Methods). We then optically pump the spin oscillator into the negative-mass configuration (c,d). Here, we demonstrate the ability to invert the direction of the phase shift of conditional squeezing while keeping all the other reference parameters unchanged. The results displayed in Fig. 3(d) correspond to the desirable configuration for quantum noise reduction in optomechanical sensors including GWDs, since the produced rotation of the squeezing phase $\Phi_-(\Omega)$ counteracts the QBA effect for a positive-mass quantum oscillator, such as an interferometer mirror. The improved conditional squeezing [as shown by the data points in (a,b)] around the Larmor frequency can be attributed to the reduced effective atomic thermal noise [34].

The phase offset $\delta\theta_i$ in the idler entangled mode due to the QWP, shown in the upper panel of Fig. 3(e), impacts the functional dependence of $\Phi(\Omega)$. The implications of rotating the quadrature basis after probing the spin ensemble are shown in the right column of Fig. 3. We highlight the downshift of the phase rotation range by ≈ 2.7 kHz and the change of the bandwidth $\delta\Omega_{\text{SQL}}$ of the squeezing rotation down to ≈ 2.5 kHz, comparing the spectrogram in Fig. 3(f) for $\delta\theta_i \approx 45^\circ$ to Fig. 3(d) where $\delta\theta_i = 0^\circ$ was set. The observed phenomenon is attributed to the *virtual rigidity* effect [37], which effectively modifies the oscillator's response to the quantum noise of the probe light as if its resonance frequency and the readout rate were changed [34], leading to $\Phi(\Omega) \rightarrow \Phi_{\text{VR}}(\Omega)$. The effect of atomic ponderomotive squeezing also alters the degree of conditional quantum noise reduction (blue data points) for different parts of the spectrum, as displayed in Fig. 3(c). Overall, the control of the phase shift $\delta\theta_i$ in the idler entangled mode provides additional flexibility for tuning the features of frequency-dependent squeezing and for corresponding optimization of the quantum noise reduction [23].

The approximation $\mathcal{K}_a \approx \Gamma_a/\Omega_a$ for the atomic coupling factor applies at $\Omega \ll |\Omega_a|$. Hence, as the Larmor frequency approaches the readout rate, the full phase rotation range for the conditional squeezing cannot be achieved for the upper (lower) range with the positive (negative) mass spin oscillator. This limitation on the phase rotation $[0^\circ, 140^\circ]$ is seen in Fig. 3(b,d), despite the increased technical noise near DC frequencies. However, the readout rate and the decay can be adjusted by carefully engineering the light-spins interaction [34].

OUTLOOK

We have demonstrated that a tunable entangled light source coupled to a spin oscillator with an adjustable oscillation frequency allows, in principle, for the reduction of both the shot noise and quantum-backaction noise of the measurement. This reduction can be achieved at

widely tunable optical wavelengths and within a broad noise frequency range. These features make our hybrid quantum system a promising candidate for the sensitivity improvement in the next generation of GWDs.

Although our current results exhibit less conditional squeezing compared to the original frequency-independent squeezing level, our model suggests that reducing the broadband spin noise by a factor of six and the spin thermal occupation by a factor of three would be sufficient to achieve the frequency-dependent squeezing level across the full bandwidth limited only by the degree of EPR correlations of light as illustrated by Extended Data Fig. 3.

With the atomic spin oscillator maintaining quantum-noise-limited performance down to the GW backaction-dominant regime, our system is analogous to the filter cavity implementations [24]. We infer that the squeezing phase rotation provided by the 8-cm-long cell in the present work is equivalent to the rotation imposed by a 5-m-long Fabry-Pérot filter cavity with finesse ~ 6000 [38], as follows from the results shown in Fig. 3(d) [see Supplementary Information]. The length of the equivalent optical cavity is effectively extended to 10 m when the virtual rigidity downshift in Fig. 3(f) is applied.

With the technical noise further suppressed and the parameters of the spin oscillator adjusted properly, the approach demonstrated here will allow to engineer the structure and spectral shape of the quantum noise to match the GWD [23]. It will open the possibility to apply the conditional frequency-dependent squeezing reported here for the sensitivity improvement beyond the SQL in the frequency range of the current GWDs.

The spin system is flexible in both its resonance frequency and bandwidth, and is scalable due to its relative compactness and simplicity. The protocol can be extended using multiple ensembles and in this way more intricate quantum noise reduction spectral profiles $\Phi(\Omega)$ within a required spectral range can be engineered. In the context of the quantum noise reduction in GWDs, a cascade of spin ensembles resembles the implementation of a cascade of filter cavities [11, 39].

The EPR source design can be adapted to link our spin oscillator with systems ranging from optomechanics to atomic physics. The required signal wavelength ranging from 700 nm to 2000 nm can be achieved by using a suitable signal laser and a corresponding nonlinear medium for parametric downconversion. Leveraging this opportunity, we envision potential applications in a broad field of quantum-enhanced metrology, such as detection of quantum motion of nanoparticles and cantilevers [40, 41], where broadband, frequency-dependent engineering of the quantum noise of light is required.

To the best of our knowledge, the demonstrated system is the first combination of multicolour continuous-variable (CV) entangled light modes with a quantum memory [42, 43], which is the backbone of proposals

for a CV quantum repeater [44]. The versatility of our hybrid network enables quantum protocols coupling efficient atom-light interfaces [45] to systems ranging from the nano to the macro scale [46, 47].

* These authors contributed equally

- [1] Tebbenjohanns, F., Mattana, M. L., Rossi, M. *et al.* Quantum control of a nanoparticle optically levitated in cryogenic free space. *Nature* **595**, 378–382 (2021). URL <http://dx.doi.org/10.1038/s41586-021-03617-w>.
- [2] Purdy, T. P., Peterson, R. W. & Regal, C. A. Observation of Radiation Pressure Shot Noise on a Macroscopic Object. *Science* **339**, 801–804 (2013). URL <http://dx.doi.org/10.1126/science.1231282>.
- [3] Acernese, F., Agathos, M., Aiello, L. *et al.* Quantum Backaction on kg-Scale Mirrors: Observation of Radiation Pressure Noise in the Advanced Virgo Detector. *Phys. Rev. Lett.* **125**, 131101 (2020). URL <https://link.aps.org/doi/10.1103/PhysRevLett.125.131101>.
- [4] Yu, H., McCuller, L., Tse, M. *et al.* Quantum correlations between light and the kilogram-mass mirrors of LIGO. *Nature* **583**, 43–47 (2020). URL <http://dx.doi.org/10.1038/s41586-020-2420-8>.
- [5] Youssefi, A., Kono, S., Chegnizadeh, M. *et al.* A squeezed mechanical oscillator with millisecond quantum decoherence. *Nature Physics* **19**, 1697–1702 (2023). URL <https://doi.org/10.1038/s41567-023-02135-y>.
- [6] Murch, K. W., Moore, K. L., Gupta, S. *et al.* Observation of quantum-measurement backaction with an ultracold atomic gas. *Nature Physics* **4**, 561–564 (2008). URL <http://dx.doi.org/10.1038/nphys965>.
- [7] Bohnet, J. G., Cox, K. C., Norcia, M. A. *et al.* Reduced spin measurement back-action for a phase sensitivity ten times beyond the standard quantum limit. *Nature Photonics* **8**, 731–736 (2014). URL <http://dx.doi.org/10.1038/nphoton.2014.151>.
- [8] Caves, C. M., Thorne, K. S., Drever, R. W. P. *et al.* On the measurement of a weak classical force coupled to a quantum-mechanical oscillator. I. Issues of principle. *Rev. Mod. Phys.* **52**, 341–392 (1980). URL <https://link.aps.org/doi/10.1103/RevModPhys.52.341>.
- [9] Braginsky, V. & Khalili, F. Quantum nondemolition measurements: the route from toys to tools. *Reviews of Modern Physics* **68** (1996). URL <https://journals.aps.org/rmp/abstract/10.1103/RevModPhys.68.1>.
- [10] Chen, Y. Macroscopic quantum mechanics: theory and experimental concepts of optomechanics. *Journal of Physics B: Atomic, Molecular and Optical Physics* **46**, 104001 (2013).
- [11] Danilishin, S. L., Khalili, F. Y. & Miao, H. Advanced quantum techniques for future gravitational-wave detectors. *Living Reviews in Relativity* **22** (2019). URL <http://dx.doi.org/10.1007/s41114-019-0018-y>.
- [12] Aslam, N., Zhou, H., Urbach, E. K. *et al.* Quantum sensors for biomedical applications. *Nature Reviews Physics* **5**, 157–169 (2023). URL <http://dx.doi.org/10.1038/s42254-023-00558-3>.
- [13] Bass, S. D. & Doser, M. Quantum sensing for particle physics. *Nature Reviews Physics* **6**, 329–339 (2024). URL <http://dx.doi.org/10.1038/s42254-024-00714-3>.
- [14] Aspelmeyer, M., Kippenberg, T. J. & Marquardt, F. Cavity optomechanics. *Rev. Mod. Phys.* **86**, 1391–1452 (2014). URL <https://link.aps.org/doi/10.1103/RevModPhys.86.1391>.
- [15] Julsgaard, B., Kozhekin, A. & Polzik, E. S. Experimental long-lived entanglement of two macroscopic objects. *Nature* **413**, 400–403 (2001). URL <http://dx.doi.org/10.1038/35096524>.
- [16] Hammerer, K., Aspelmeyer, M., Polzik, E. S. *et al.* Establishing Einstein-Poldosky-Rosen Channels between Nanomechanics and Atomic Ensembles. *Phys. Rev. Lett.* **102**, 020501 (2009). URL <https://link.aps.org/doi/10.1103/PhysRevLett.102.020501>.
- [17] Tsang, M. & Caves, C. M. Coherent Quantum-Noise Cancellation for Optomechanical Sensors. *Phys. Rev. Lett.* **105**, 123601 (2010). URL <https://link.aps.org/doi/10.1103/PhysRevLett.105.123601>.
- [18] Tsang, M. & Caves, C. M. Evading Quantum Mechanics: Engineering a Classical Subsystem within a Quantum Environment. *Phys. Rev. X* **2**, 031016 (2012). URL <https://link.aps.org/doi/10.1103/PhysRevX.2.031016>.
- [19] Møller, C. B., Thomas, R. A., Vasilakis, G. *et al.* Quantum back-action-evading measurement of motion in a negative mass reference frame. *Nature* **547**, 191–195 (2017). URL <http://dx.doi.org/10.1038/nature22980>.
- [20] Thomas, R. A., Parniak, M., Østfeldt, C. *et al.* Entanglement between distant macroscopic mechanical and spin systems. *Nature Physics* **17**, 228–233 (2021). URL <http://dx.doi.org/10.1038/s41567-020-1031-5>.
- [21] Mercier de Lépinay, L., Ockeloen-Korppi, C. F., Woolley, M. J. *et al.* Quantum mechanics-free subsystem with mechanical oscillators. *Science* **372**, 625–629 (2021). URL <http://dx.doi.org/10.1126/science.abf5389>.
- [22] Khalili, F. Y. & Polzik, E. S. Overcoming the Standard Quantum Limit in Gravitational Wave Detectors Using Spin Systems with a Negative Effective Mass. *Phys. Rev. Lett.* **121**, 031101 (2018). URL <https://link.aps.org/doi/10.1103/PhysRevLett.121.031101>.
- [23] Zeuthen, E., Polzik, E. S. & Khalili, F. Y. Gravitational wave detection beyond the standard quantum limit using a negative-mass spin system and virtual rigidity. *Phys. Rev. D* **100**, 062004 (2019). URL <https://link.aps.org/doi/10.1103/PhysRevD.100.062004>.
- [24] Ganapathy, D., Jia, W., Nakano, M. *et al.* Broadband Quantum Enhancement of the LIGO Detectors with Frequency-Dependent Squeezing. *Phys. Rev. X* **13**, 041021 (2023). URL <https://link.aps.org/doi/10.1103/PhysRevX.13.041021>.
- [25] Acernese, F., Agathos, M., Ain, A. *et al.* Frequency-Dependent Squeezed Vacuum Source for the Advanced Virgo Gravitational-Wave Detector. *Phys. Rev. Lett.* **131**, 041403 (2023). URL <https://link.aps.org/doi/10.1103/PhysRevLett.131.041403>.
- [26] Jia, W. *et al.* Squeezing the quantum noise of a gravitational-wave detector below the standard quantum limit. *Science* **385**, 1318–1321 (2024).
- [27] Kimble, H. J., Levin, Y., Matsko, A. B. *et al.* Conversion of conventional gravitational-wave interferometers into quantum nondemolition interferometers by modifying their input and/or output optics. *Phys. Rev. D* **65**, 022002 (2001). URL <https://link.aps.org/doi/10.1103/PhysRevD.65.022002>.

- [28] Jones, P., Zhang, T., Miao, H. *et al.* Implications of the quantum noise target for the Einstein Telescope infrastructure design. *Phys. Rev. D* **101**, 082002 (2020). URL <https://link.aps.org/doi/10.1103/PhysRevD.101.082002>.
- [29] Ma, Y., Miao, H., Pang, B. H. *et al.* Proposal for gravitational-wave detection beyond the standard quantum limit through EPR entanglement. *Nature Physics* **13**, 776–780 (2017). URL <http://dx.doi.org/10.1038/nphys4118>.
- [30] Nishino, Y., Danilishin, S., Enomoto, Y. *et al.* Frequency-dependent squeezing for gravitational-wave detection through quantum teleportation. *Phys. Rev. A* **110**, 022601 (2024). URL <https://link.aps.org/doi/10.1103/PhysRevA.110.022601>.
- [31] Brown, D. D., Miao, H., Collins, C. *et al.* Broadband sensitivity enhancement of detuned dual-recycled Michelson interferometers with EPR entanglement. *Phys. Rev. D* **96**, 062003 (2017). URL <https://link.aps.org/doi/10.1103/PhysRevD.96.062003>.
- [32] Peng, X., Martynov, D., Zhu, Z. *et al.* Approaches of frequency-dependent squeezing for the low frequency detector of the Einstein Telescope. *Phys. Rev. D* **110**, 082006 (2024). URL <https://link.aps.org/doi/10.1103/PhysRevD.110.082006>.
- [33] Reid, M. D. Demonstration of the Einstein-Podolsky-Rosen paradox using nondegenerate parametric amplification. *Phys. Rev. A* **40**, 913–923 (1989). URL <https://link.aps.org/doi/10.1103/PhysRevA.40.913>.
- [34] Jia, J., Novikov, V., Brasil, T. B. *et al.* Acoustic frequency atomic spin oscillator in the quantum regime. *Nature Communications* **14** (2023). URL <http://dx.doi.org/10.1038/s41467-023-42059-y>.
- [35] Borregaard, J., Davis, E., Bentsen, G. S., Schleier-Smith, M. H. & Sørensen, A. S. One-and two-axis squeezing of atomic ensembles in optical cavities. *New Journal of Physics* **19**, 093021 (2017).
- [36] Kitagawa, M. & Ueda, M. Squeezed spin states. *Physical Review A* **47**, 5138 (1993).
- [37] Danilishin, S. L. & Khalili, F. Y. Quantum Measurement Theory in Gravitational-Wave Detectors. *Living Reviews in Relativity* **15** (2012). URL <http://dx.doi.org/10.12942/lrr-2012-5>.
- [38] McCuller, L., Whittle, C., Ganapathy, D. *et al.* Frequency-Dependent Squeezing for Advanced LIGO. *Phys. Rev. Lett.* **124**, 171102 (2020). URL <https://link.aps.org/doi/10.1103/PhysRevLett.124.171102>.
- [39] Buonanno, A. & Chen, Y. Quantum noise in second generation, signal-recycled laser interferometric gravitational-wave detectors. *Phys. Rev. D* **64**, 042006 (2001). URL <https://link.aps.org/doi/10.1103/PhysRevD.64.042006>.
- [40] Gonzalez-Ballesteros, C., Zielińska, J., Rossi, M. *et al.* Suppressing Recoil Heating in Levitated Optomechanics Using Squeezed Light. *PRX Quantum* **4**, 030331 (2023). URL <https://link.aps.org/doi/10.1103/PRXQuantum.4.030331>.
- [41] Yap, M. J., Cripe, J., Mansell, G. L. *et al.* Broadband reduction of quantum radiation pressure noise via squeezed light injection. *Nature Photonics* **14**, 19–23 (2020).
- [42] Julsgaard, B., Sherson, J., Cirac, J. I., Fiurášek, J. & Polzik, E. S. Experimental demonstration of quantum memory for light. *Nature* **432**, 482–486 (2004). URL <http://dx.doi.org/10.1038/nature03064>.
- [43] Jensen, K. *et al.* Quantum memory for entangled continuous-variable states. *Nature Physics* **7**, 13–16 (2010). URL <http://dx.doi.org/10.1038/nphys1819>.
- [44] Dias, J., Winnel, M. S., Hosseinidehaj, N. *et al.* Quantum repeater for continuous-variable entanglement distribution. *Phys. Rev. A* **102**, 052425 (2020). URL <https://link.aps.org/doi/10.1103/PhysRevA.102.052425>.
- [45] Hammerer, K., Sørensen, A. S. & Polzik, E. S. Quantum interface between light and atomic ensembles. *Reviews of Modern Physics* **82**, 1041–1093 (2010).
- [46] Kimble, H. J. The quantum internet. *Nature* **453**, 1023–1030 (2008). URL <http://dx.doi.org/10.1038/nature07127>.
- [47] Wehner, S., Elkouss, D. & Hanson, R. Quantum internet: A vision for the road ahead. *Science* **362** (2018). URL <http://dx.doi.org/10.1126/science.aam9288>.
- [48] Brasil, T. B., Novikov, V., Kerdoncuff, H. *et al.* Two-colour high-purity Einstein-Podolsky-Rosen photonic state. *Nature Communications* **13** (2022). URL <http://dx.doi.org/10.1038/s41467-022-32495-7>.
- [49] Novikov, V. *et al.* Coherent phase control of two-color Einstein-Podolsky-Rosen photonic state. *In Preparation* (2025).
- [50] Grimaldi, A. *et al.* Two-color Einstein-Podolsky-Rosen state at sub-kHz regime. *In Preparation* (2025).
- [51] Borregaard, J., Zugenmaier, M., Petersen, J. *et al.* Scalable photonic network architecture based on motional averaging in room temperature gas. *Nature communications* **7**, 11356 (2016).
- [52] Shaham, R., Katz, O. & Firstenberg, O. Quantum dynamics of collective spin states in a thermal gas. *Phys. Rev. A* **102**, 012822 (2020). URL <https://link.aps.org/doi/10.1103/PhysRevA.102.012822>.
- [53] Schori, C., Sørensen, J. L. & Polzik, E. S. Narrow-band frequency tunable light source of continuous quadrature entanglement. *Phys. Rev. A* **66**, 033802 (2002). URL <https://link.aps.org/doi/10.1103/PhysRevA.66.033802>.
- [54] Luis, A. & Korolkova, N. Polarization squeezing and nonclassical properties of light. *Phys. Rev. A* **74**, 043817 (2006). URL <https://link.aps.org/doi/10.1103/PhysRevA.74.043817>.
- [55] Bowen, W. P., Schnabel, R., Bachor, H.-A. *et al.* Polarization squeezing of continuous variable stokes parameters. *Physical Review Letters* **88**, 093601 (2002).
- [56] Gould, D. W. *et al.* Optimal quantum noise cancellation with an entangled witness channel. *Physical Review Research* **3**, 043079 (2021).

METHODS

A detailed layout of the experimental setup is shown in Extended Data Fig. 1. Below we discuss the main components of the system and their characterization.

EPR source

As shown in Extended Data Fig. 1, two lasers at 852 nm (Msquared - Solstis) and 1064 nm (Innolight - Mephisto) drive the Sum-Frequency-Generation (SFG)

producing the pump beam at 473 nm for a Nondegenerate Optical Parametric Oscillator (NOPO) which generates the EPR state of light. The NOPO cavity design and the operation principle are reported in Ref. [48]. The cavity has a bow-tie configuration with a Periodically Poled Potassium Titanyl Phosphate (PPKTP) nonlinear crystal. The resonance of the NOPO for the 852 nm and 1064 nm downconverted modes is maintained by locking the cavity to the 1064 nm laser and locking the 852 nm laser to the cavity, using beams counter-propagating to the EPR modes. To achieve the quantum noise limited performance in the audio frequency band required in the present paper, we have implemented the reduction of classical noise contamination on our probe laser using an active noise eater and have achieved robust control of the EPR state phases, as described in depth in Ref [49].

The EPR output modes of the NOPO cavity are separated by a dichroic mirror. The signal mode at 1064 nm is mixed with the corresponding LO_s on a 50:50 beam splitter, and the canonical operators (x_s, p_s) are measured using a balanced homodyne detector HDs (Extended Data Fig. 1). The 852 nm idler mode is combined with an orthogonally polarized probe beam LO_i on a polarizing beam splitter (PBS) and polarization homodyning is performed.

We observe 9 dB of two-mode squeezing, corresponding to 6 dB of conditional squeezing on the signal mode when the two EPR modes are analysed directly (the idler bypasses the atoms) [50]. The electronic noise floor is more than 17 dB below the shot noise level.

Prior to entering the atomic ensemble, the combined idler mode and LO_i are shaped into a square top-hat profile, enabling the optimal readout of atomic spins (see the subsection on characterization of the spin oscillator). To characterize the overall propagation losses, including those from the cell windows, beam shaper and optics, a measurement with the Larmor frequency tuned to 1 MHz, beyond the detection frequency band, has been performed. We still observe ~ 3.3 dB conditional squeezing from 3 kHz to 60 kHz relative to the signal vacuum noise, as shown in the upper panel (a) of Extended Data Fig. 2. Noise peaks at 26 kHz and 36 kHz are experimental artefacts caused by the intensity noise eater. The theory of the conditional squeezing, detailed in the supplementary material (or reference), allows us to extrapolated a squeezing factor $r = 1.42$ and unbalanced detection efficiency of $\eta_s \sim 0.92$ for the signal arm and $\eta_i = \eta_{i,out}\eta_{i,in} \sim 0.8$ for the idler arm by fitting the measured power spectrum densities. See the parameters table below for more details.

Atomic spin oscillator

The atomic spin oscillator is implemented by confining a gas of $N_{Cs} \sim 10^{10}$ ^{133}Cs atoms in a $2 \times 2 \times 80$ mm³ glass

channel inside a vapour cell. The cell windows are anti-reflection coated and the inner walls are coated with an anti-relaxation paraffin material to minimize the decoherence from spin-wall collisions. The glass cell, including the stem, is heated to $\sim 40^\circ\text{C}$ to ensure sufficient atomic density. A multilayer magnetic shield around the cell provides isolation from the Earth's magnetic field and other high-frequency magnetic noise, while a set of coils running low-noise DC currents generates a highly homogeneous bias magnetic field within the cell. By adjusting the DC current, we can control the Larmor frequency $|\Omega_a|$ from 1 MHz down to 3 kHz, maintaining quantum-dominated performance throughout this frequency spectrum [34].

As depicted in Extended Data Fig. 1, the vapour cell is illuminated by two optical fields. A circularly polarized optical repumping field, propagating transversely, prepares the spin ensemble in the hyperfine $|F = 4, m_F = 4\rangle$ or $|F = 4, m_F = -4\rangle$ ground state manifold with 82% efficiency, enabling it to function as a macroscopic spin oscillator with an adjustable sign of the effective mass.

The probe beam is blue-detuned by 1.6 GHz from the D2 line $F = 4 \rightarrow F' = 5$ transition to eliminate the absorption. The polarization of the probe entering the atomic ensemble is chosen to optimize the light-spin interaction as discussed in the main text [20, 34]. The light-atoms interaction strength, characterized by the readout rate Γ_a , is controlled by the power of the probe laser, its detuning from the D2 line, and by the number of atomic spins N_{Cs} . The spin oscillator experiences depolarization, primarily due to the spontaneous emission induced by the probe field. This leads to the spin thermal noise imprinted onto the output probe beam. In the regime of strong light-atom coupling $\Gamma_a \gg \gamma_a$, the quantum back-action induced by the probe dominates over the atomic thermal noise. Atoms that maintain interaction with the probe by multiple passages during the coherent evolution time contribute to the narrow-band atomic response limited by the spin decoherence rate γ_a . The remaining atoms contribute to faster-decaying atomic modes leading to additional, broadband atomic noise with the bandwidth of $\gamma_{bb} \gg \gamma_a$ [20, 51, 52]. To minimise the broadband noise, the input field, comprising two orthogonally polarized modes (idler and LO_i), is shaped into a collimated square top-hat beam with a 7th-order super-Gaussian waist of 1.7 mm by the top-hat shaper (THS) as shown in the Extended Data Fig. 1. It propagates through the cell with the filling factor $\sim 80\%$ without introducing extra losses. The effect of the remaining broadband noise is illustrated in Extended Data Fig. 2.

To characterise the spin oscillator, we block the idler EPR mode and drive the atoms with a coherent state of light. The Larmor frequency is set to $\Omega_a/2\pi \sim 10.5$ kHz and the quadrature of the output probe light is adjusted by a quarter- and a half-wave plate. In Extended Data Fig. 2(b), the recorded quantum noise, dominated by

the spin quantum-backaction noise (QBAN) is shown as the red area. Choosing an optimal polarization of detected light we observe 5 dB of ponderomotive squeezing, as shown in the upper left inset of the figure. By fitting the displayed spin noise spectra, we can extract both the narrowband and broadband spin readout and decay rates along with the losses after the spin ensemble and the effective thermal occupancies (see Extended Data Table I). The extracted occupancy number greater than 1.5 estimated from imperfect spin polarization using MORS measurement, is due to contributions from other environmental noise sources, which add uncorrelated noise and degrade the degree of squeezing. The effective thermal occupancies for the narrow band and broadband spin responses are the same. The reconstructed atomic thermal noise (the light blue area) and broadband noise (the purple area) are also presented in the Fig. 2(b). The impact of these distinct spectral features on the conditional frequency-dependent squeezing level is discussed below. The red area, representing the quantum-backaction noise, highlights the key quantum contribution that enables the frequency-dependent rotation of the squeezing phase. The same calibration procedure was applied to experimental data at 54 kHz Larmor frequency, demonstrated in Extended Data Fig. 2. The reduced classical noise at this frequency band allowed for better fitting.

After characterizing the spin oscillator, we unblock the idler output of the NOPO and record the dynamics of the spin oscillator driven by the idler component of the EPR field. The virtual rigidity phase $\delta\theta_i$ is extracted by fitting the noise spectrum shown in the right inset of Fig. 2(b) (green trace). By combining the overall losses obtained from the EPR source calibration with the optical and detection losses after atoms evaluated from ponderomotive squeezing, we estimate the propagation efficiency between the NOPO and atoms to be of $\eta_{i,\text{in}} \sim 89\%$. The optical losses from the atoms to the detection in the idler arm have been measured and result in the efficiency $\eta_{i,\text{out}} \sim 90\%$. Propagation efficiency from the NOPO and the detection efficiency in the signal arm result in $\eta_s \sim 92\%$. Based on those numbers, the predicted degree of two-mode squeezing fits the observed degree of squeezing as shown in Extended Data Fig. 2.

Using the parameters extracted from these independent calibrations and the model presented in the next sections, Eq. (10), we calculate the predicted frequency-dependent conditional squeezing as a function of the signal homodyne angle θ_s shown in Figs. 2 and 3 of the main text. The figures show good agreement between the predicted spectra of quantum noise with the experimental data.

Phase control of the signal and idler modes

A feature of the EPR source critical for the present work is a phase control of the two-colour EPR state. Here we describe its underlying principles, while a complete report is in preparation [49]. The phases of the signal and idler beams of the NOPO are related to the pump phase by $\theta_p = \phi_i + \phi_s$ [33, 53]. To be able to precisely track the phase of the signal and the idler, we inject a coherent α_c beam, co-propagating with the pump and frequency-shifted by $\delta\omega_c$ from the 1064 nm laser by two Acousto-Optic Modulators (AOMs).

In this experiment we choose $\delta\omega_c/2\pi = 3$ MHz, well inside the NOPO cavity bandwidth, but also far from the resonance of the atomic spin oscillator. An electronic reference phase for the control beam ϕ_c is provided by driving the AOMs by two outputs of a ultra-low phase noise Direct Digital Synthesizer (DDS).

The control beam experiences the parametric interaction and is amplified while maintaining its phase. The interaction of control and pump provides the simultaneous generation of another coherent field centred at frequency $\omega_i - \delta\omega_c$. In this case, the field phase is the combination of the pump and signal control beam phases, $\phi_c^i = \theta_p - \phi_c$. The classical beams generated by this process propagate together with their respective entangled modes to the homodyne detections. We demodulate the photocurrents using the electronic reference. This provides an error signal proportional to the phase difference between the entangled modes and the local oscillators, measured by the two homodyne detectors (HDs). The photocurrent from HDs $I_s(t)$ contains the information from the signal mode quadrature and the beatnote of the local oscillator with the amplified control field on the wavelength λ_s .

$$I_s(t) \propto q_s(\theta_s) + \alpha_c^s \cos(\delta\omega_c t - \phi_c), \quad (5)$$

allowing us to select and set the homodyne phase θ_s . In turn, the outcome of the measurement of the idler mode by means of the homodyne detection can be presented as

$$I_i(t) \propto Q_i(\theta_i) + \alpha_c^i \cos(\delta\omega_c t - \phi_c^i - \phi_i), \quad (6)$$

where the second term on the right side is the beat note between the second coherent field exiting NOPO and the respective local oscillator. Similarly, it provides a tool to control the homodyne phase $\theta_i = \phi_i + \delta\theta_i$, whereas the phase offset $\delta\theta_i$ can be tuned separately using the quarter-wave plate (see the setup in Extended Data Fig. 1 and Fig. 1 in the main text).

The frequency offset of $\delta\omega_c/2\pi \simeq 3$ MHz, guarantees that locking of those phases is not affected by the atomic spin oscillator. The procedure described above provides a set of well-defined phases that we use as references for the scan of θ_s involved in the demonstration of frequency-dependent conditional squeezing.

Idler mode and light-atoms interaction

The 1.6 GHz detuning of the 852 nm NOPO idler mode from atomic resonance is achieved by changing the frequency of the 1064 nm laser, which alters the NOPO cavity length and its resonance condition. The 852 nm laser lock follows the change, enabling fine-tuning of the idler mode with precision close to the NOPO cavity bandwidth.

To enable interaction between the idler mode and the atomic spin ensemble, we overlap the idler output of the NOPO with an orthogonally polarized probe beam. This is realised by combining the linearly polarised idler and probe beams on a Polarising Beam Splitter (PBS), which transforms the idler mode's quadrature fluctuations into Stokes operator fluctuations [19, 54, 55]. For a linearly polarised, strong coherent probe beam with a relative phase ϕ_i between the idler and the probe, the quadratures map onto the Stokes operators as $q_i(\phi_i) = \sqrt{2}\mathcal{S}_3/|\alpha_{pr}|$ and $q_i(\phi_i + \pi/2) = \sqrt{2}\mathcal{S}_2/|\alpha_{pr}|$, where α_{pr} is the amplitude of the probe field, $\{\mathcal{S}_0, \mathcal{S}_1, \mathcal{S}_2, \mathcal{S}_3\}$ are quantum Stokes operators and $q_i(\phi_i) = \cos(\phi_i)p_i + \sin(\phi_i)x_i$ is the quadrature of the optical mode entering the atomic ensemble.

The idler mode encoded into the polarisation state is processed by the atomic ensemble. The output Stokes parameters are then given by $\mathcal{S}_3^{\text{out}} = \mathcal{S}_3^{\text{in}}$ and $\mathcal{S}_2^{\text{out}} = \mathcal{S}_2^{\text{in}} + \mathcal{K}_a \mathcal{S}_3^{\text{in}} + \mathcal{N}_a$, where $\mathcal{N}_a = N_a |\alpha_{pr}|/\sqrt{2}$; \mathcal{K}_a and N_a are defined in the main text.

The light emerging from the spin ensemble is measured by the polarization homodyne detection. The diagonal linear and circular polarization operators \mathcal{S}_2 and \mathcal{S}_3 are measured by passing light through a half-wave plate, and an additional Quarter-Wave Plate (QWP), respectively, followed by the PBS, as shown in the Extended Data Fig. 1. The resulting photocurrent is proportional to $Q_i = \mathcal{S}_3^{\text{out}} \cos(\delta\theta_i) + \mathcal{S}_2^{\text{out}} \sin(\delta\theta_i)$, where the phase $\delta\theta_i$ is set by the orientation of the QWP.

The phase ϕ_i is set by a coherent control loop that monitors the phase offset between the probe beam and the control field at the idler homodyne detector. The control field follows the same propagation path as the idler beam, but is unaffected by the atomic oscillator due to a frequency offset, $\delta\omega_{\text{cfl}}$. The phase offset ϕ_i measured by the coherent control loop combines the encoding phase and $\delta\theta_i$.

Throughout those measurements, we set $\theta_i = 0$, so that the quadrature of the idler detected outside the bandwidth of the spin dynamics bandwidth ($\Omega \gg |\Omega_a|$) is p_i . In the setting not engaging virtual rigidity, that is in the absence of QWP ($\delta\theta_i = 0$), the coherent control loop sets the encoding phase $\phi_i = 0$, corresponding to $\mathcal{S}_2^{\text{in}} = x_i |\alpha_{pr}|/\sqrt{2}$ and $\mathcal{S}_3^{\text{in}} = p_i |\alpha_{pr}|/\sqrt{2}$. With such settings, the final idler photocurrent is $q_i = Q_i \sqrt{2}/|\alpha_{pr}| = p_i + \mathcal{K}_a(\Omega)x_i + N_a(\Omega)$.

Optimal quantum noise reduction by Wiener filtering in the idler channel

The squeezing we demonstrate for the signal arm is conditioned on the idler-arm measurement

$$Q_{s|i}(\Omega, \theta_s) = q_s(\Omega, \theta_s) + g(\Omega, \theta_s, \delta\theta_i)q_i(\Omega, \delta\theta_i). \quad (7)$$

To achieve the maximal frequency-dependent squeezing of the signal mode based on the idler measurement record, a Wiener filter $g(\Omega, \theta_s, \delta\theta_i)$ is designed for each detection phase θ_s , which provides an optimal estimate of the correlated quantum noise in the idler channel. By subtracting the filtered idler quantum noise from the signal noise, the optimal reduction of the signal quantum noise limited by the remaining uncorrelated noise is achieved [11, 29, 56].

Our protocol is compatible with both causal and non-causal filtering $g(\Omega, \theta_s, \delta\theta_i)$ of the idler measurement record. Causal filtering, which uses only past idler measurements to reduce the signal arm noise at a given time, is required for using the sensor for, e.g., real-time signal tracking or adaptive sensing. On the other hand, the non-causal filtering uses the full idler measurement record and is relevant for sensing scenarios where the signal is extracted by post-processing of the full measurement record.

In this work we focus on non-causal conditioning, thereby emphasizing the maximally achievable squeezing. In this case, the optimal gain is given by the idler spectral density S_{q_i} and the cross-spectral density S_{q_s, q_i} of the two entangled channels as

$$g(\Omega, \theta_s, \delta\theta_i) = -\frac{S_{q_s, q_i}(\Omega, \theta_s, \delta\theta_i)}{S_{q_i}(\Omega, \delta\theta_i)} \quad (8)$$

which leads to the power spectral density of the optimised signal

$$S_{Q_{s|i}}(\Omega, \theta_s) = S_{q_s}(\Omega, \theta_s) - \frac{|S_{q_s, q_i}(\Omega, \theta_s, \delta\theta_i)|^2}{S_{q_i}(\Omega, \delta\theta_i)}. \quad (9)$$

The optimal filter (8) automatically takes into account the signal homodyne detection phase θ_s , deleterious noise introduced in the idler path, and phase shifts due to the atomic dissipation through decoherence, as represented by the complexity of the response function $\mathcal{K}_a(\Omega)$ (see Eq. (2) in the main text). Additionally, the Wiener filter can potentially compensate for imperfect matching between the idler and the quantum sensor response introduced in the signal arm in a particular sensing application. The analysis of the experimental data using this approach is detailed in the SI.

Theory of frequency-dependent conditional squeezing

Figs. 2 and 3 in the main text present comparisons of the measured squeezing with the theoretical model, which we describe here. The model consists of equations of motion of the spin oscillator and input-output relations describing its interaction with light. It accounts for contributions of thermal and broadband noise to the response of the spin system, as well as for the effects of imperfect readout efficiency ($\eta_{i,\text{out}} < 1$), imperfect coupling of the idler beam to the oscillator ($\eta_{i,\text{in}} < 1$) and the readout efficiency in the signal arm, $\eta_s < 1$. From this model we obtain an expression for the power spectral density of the conditioned signal photocurrent $Q_{s|i}$, which, in turn, is minimized using Wiener filter theory as outlined in the preceding Methods subsection. Detailed calculations are provided in the SI.

Here we present a general formula for an arbitrary phase offset $\delta\theta_i$ imposed by the quarter-wave plate and giving rise to virtual rigidity. The case of no virtual rigidity can be obtained by setting $\delta\theta_i = 0$. The spectrum of the optimally conditioned signal, normalised to the signal shot noise S_{SN} level, in the signal-arm detection quadrature θ_s is given by

$$\frac{S_{Q_{s|i}}}{S_{SN}} = 1 - \eta_s + \frac{\eta_s}{\cosh(2r)} \times \left[\cosh^2(2r) - \frac{\sinh^2(2r) |\cos(\theta_s) - \sin(\theta_s) \mathcal{K}_a^{\text{eff}}|^2}{1 + |\mathcal{K}_a^{\text{eff}}|^2 + 2 \frac{\Lambda_{\text{in}}^{\text{eff}} + \Lambda_{\text{out}}^{\text{eff}} + S_{\text{th}}^{\text{eff}} + S_{\text{bb}}^{\text{eff}}}{\eta_{i,\text{in}} \cosh(2r)}} \right], \quad (10)$$

where dependencies on Ω are omitted for brevity. The numerator of the second term in the brackets represents the correlation between the signal and idler, shaped by the backaction of the atomic spin oscillator. The denominator captures the spectrum of the idler signal, incorporating, in addition to the backaction, the following four terms, responsible for the various deleterious effects mentioned above,

$$\Lambda_{\text{in}}^{\text{eff}}(\Omega) = \frac{1 - \eta_{i,\text{in}}}{2} (1 + |\mathcal{K}_a^{\text{eff}}(\Omega)|^2) \quad (11)$$

$$\Lambda_{\text{out}}^{\text{eff}}(\Omega) = \frac{1 - \eta_{i,\text{out}}}{2\eta_{i,\text{out}}} \frac{1}{|g_{\text{VR}}(\Omega)|^2} \quad (12)$$

$$S_{\text{th}}^{\text{eff}}(\Omega) = \left| \mathcal{K}_{\text{th}}(\Omega) \frac{\cos(\delta\theta_i)}{g_{\text{VR}}(\Omega)} \right|^2 (1/2 + n_{\text{th}}) \quad (13)$$

$$S_{\text{bb}}^{\text{eff}}(\Omega) = \left| \mathcal{K}_{\text{bb}}(\Omega) \frac{\cos(\delta\theta_i)}{g_{\text{VR}}(\Omega)} \right|^2 (1/2 + n_{\text{bb}}). \quad (14)$$

In order of appearance, they represent the effects of sub-optimal coupling of the idler mode to the spin ensemble, $\eta_{i,\text{in}}$, imperfect readout efficiency of the idler detector, $\eta_{i,\text{out}}$, thermal occupation of the collective spin state, n_{th} , governed by $\mathcal{K}_{\text{th}}(\Omega) = \sqrt{2\gamma_a \Gamma_a} \Omega_a / (\Omega_a^2 - \Omega^2 - i\gamma_a \Omega + \gamma_a^2/4)$

and the broadband noise occupation number, n_{bb} , governed by $\mathcal{K}_{\text{bb}}(\Omega) = \sqrt{2\gamma_{\text{bb}} \Gamma_{\text{bb}}} \Omega_a / (\Omega_a^2 - \Omega^2 - i\gamma_{\text{bb}} \Omega + \gamma_{\text{bb}}^2/4)$. The effect of the *virtual rigidity* is captured by the gain

$$g_{\text{VR}}(\Omega) = 1 + \mathcal{K}_a(\Omega, \Omega_a, \Gamma_a) \frac{\sin(2\delta\theta_i)}{2}. \quad (15)$$

The effective backaction $\mathcal{K}_a^{\text{eff}}(\Omega) \equiv \mathcal{K}_a(\Omega, \Omega_a^{\text{eff}}, \Gamma_a^{\text{eff}})$ is defined as the backaction coefficient used in Eq. (2) of the main text, but evaluated with the effective readout rate and the effective Larmor frequency

$$\Gamma_a^{\text{eff}} = \Gamma_a \frac{\cos^2(\delta\theta_i)}{\sqrt{1 - \frac{\Gamma_a}{2\Omega_a} \sin(2\delta\theta_i)}} \quad (16)$$

$$\Omega_a^{\text{eff}} = \Omega_a \sqrt{1 - \frac{\Gamma_a}{2\Omega_a} \sin(2\delta\theta_i)}. \quad (17)$$

By minimizing Eq. (10) as a function of θ_s for each Fourier component Ω separately, we find the optimal angle $\theta_s = \Phi_{\text{VR}}(\Omega)$ to be the solution to the set of equations

$$\tan(2\Phi_{\text{VR}}(\Omega)) = \frac{-2\text{Re}[(\mathcal{K}_a^{\text{eff}}(\Omega))^{-1}]}{|\mathcal{K}_a^{\text{eff}}(\Omega)|^{-2} - 1} \quad (18a)$$

$$\text{sign}[\cos(2\Phi_{\text{VR}}(\Omega))] = \text{sign}(1 - |\mathcal{K}_a^{\text{eff}}(\Omega)|^2) \quad (18b)$$

In the limit $\gamma_a^2 \ll (\Omega_a^{\text{eff}})^2, (\Gamma_a^{\text{eff}})^2$ we have $|\mathcal{K}_a^{\text{eff}}(\Omega)|^{-2} \approx \text{Re}^2[(\mathcal{K}_a^{\text{eff}}(\Omega))^{-1}] \approx [(\mathcal{K}_a^{\text{eff}}(\Omega))^{-1}]_{\gamma_a \rightarrow 0}^2$, whereby Eqs. (18) reduce to

$$\Phi_{\text{VR}}(\Omega) \approx -\arctan(\mathcal{K}_a^{\text{eff}}(\Omega))|_{\gamma_a \rightarrow 0} \quad (19)$$

as presented in the main text. This expression, valid for general $\delta\theta_i$, is used to generate the dashed curves presented as $\Phi_j(\Omega)$ in the main text Figs. 2(b) and 3(b,d,f) for the various special cases labelled $j \in \{\pm, \text{VR}\}$. Evaluating Eq. (10) at $\theta_s = \Phi_{\text{VR}}(\Omega)$ yields the achieved degree of (frequency-dependent) squeezing; this amounts to replacing the factor

$$|\cos(\theta_s) - \sin(\theta_s) \mathcal{K}_a^{\text{eff}}|^2 \rightarrow \frac{1 + |\mathcal{K}_a^{\text{eff}}|^2}{2} \left[1 + \sqrt{1 - \frac{4\text{Im}^2[\mathcal{K}_a^{\text{eff}}]}{(1 + |\mathcal{K}_a^{\text{eff}}|^2)^2}} \right] \approx 1 + |\mathcal{K}_a^{\text{eff}}|^2, \quad (20)$$

where the approximation is valid in the limit $\gamma_a^2 \ll (\Omega_a^{\text{eff}})^2, (\Gamma_a^{\text{eff}})^2$.

In the aforementioned limit, we may use Eqs. (2) and (19) to derive an expression for the bandwidth $\delta\Omega_{\text{SQL}} > 0$ over which the rotation angle $\Phi(\Omega) \in [0, \pi]$ for specificity) changes by 45° relative to its value at the effective spin oscillator resonance $\Phi(\Omega_a^{\text{eff}}) = \pi/2$, i.e., that obeys $|\Phi(\Omega_a^{\text{eff}} + \delta\Omega_{\text{SQL}}) - \Phi(\Omega_a^{\text{eff}})| = \pi/4$. The result is $\delta\Omega_{\text{SQL}} = |\Omega_a^{\text{eff}}| (\sqrt{1 + \Gamma_a^{\text{eff}}/|\Omega_a^{\text{eff}}|} - 1) \approx \Gamma_a^{\text{eff}}/2$, where the approximation holds under the additional assumption $\Gamma_a^{\text{eff}} \ll |\Omega_a^{\text{eff}}|$.

In addition to comparing our model to the squeezing achieved in the present experiment, we also used the model to predict the degree of broadband noise reduction obtained by reducing the two main imperfections of our system: broadband spin noise and thermal spin noise. The results are reported in Extended Data Fig. 3, while further details can be found in the SI.

ACKNOWLEDGMENTS

This work has been supported by VILLUM FONDEN under a Villum Investigator Grant, grant no. 25880, by the Novo Nordisk Foundation through Copenhagen Center for Biomedical Quantum Sensing, grant number NNF24SA0088433, by the European Union’s Horizon 2020 research and innovation program under the Marie Skłodowska-Curie grant agreements No. 125101 ‘EPROXY’ and No. 122436 QNOIWA, and the European Research Council Advanced grant QUANTUM-N. We acknowledge Alkiviadis Zoumis and Ryan Yde for their experimental contributions. T.B.B., J.J., V.N. and E.S.P. acknowledge valuable discussions with Jürgen Appel, Mikael Lassen, Farid Khalili, Rodrigo Thomas and

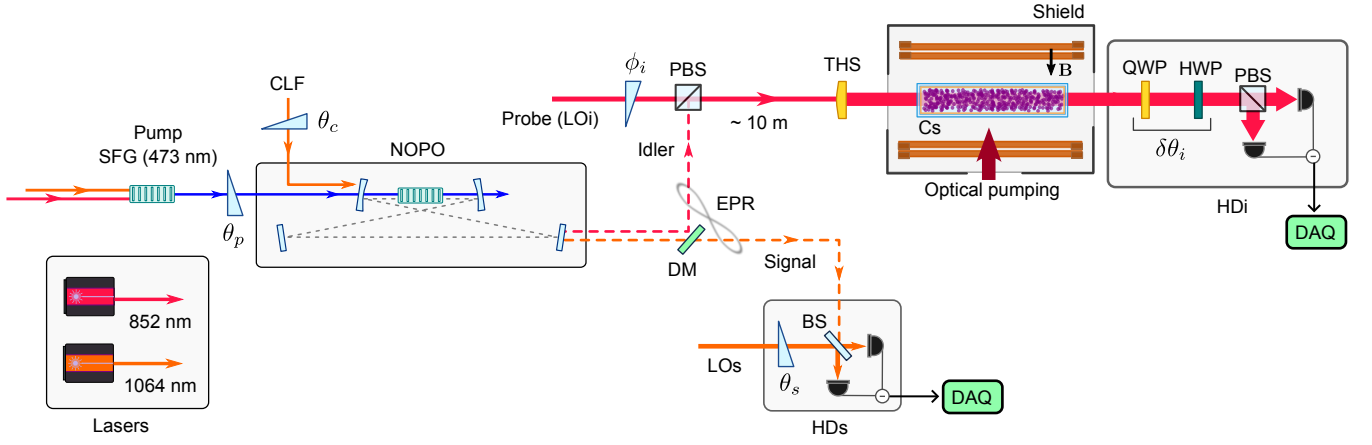
Michał Parniak at the early stages of this project.

AUTHOR CONTRIBUTIONS

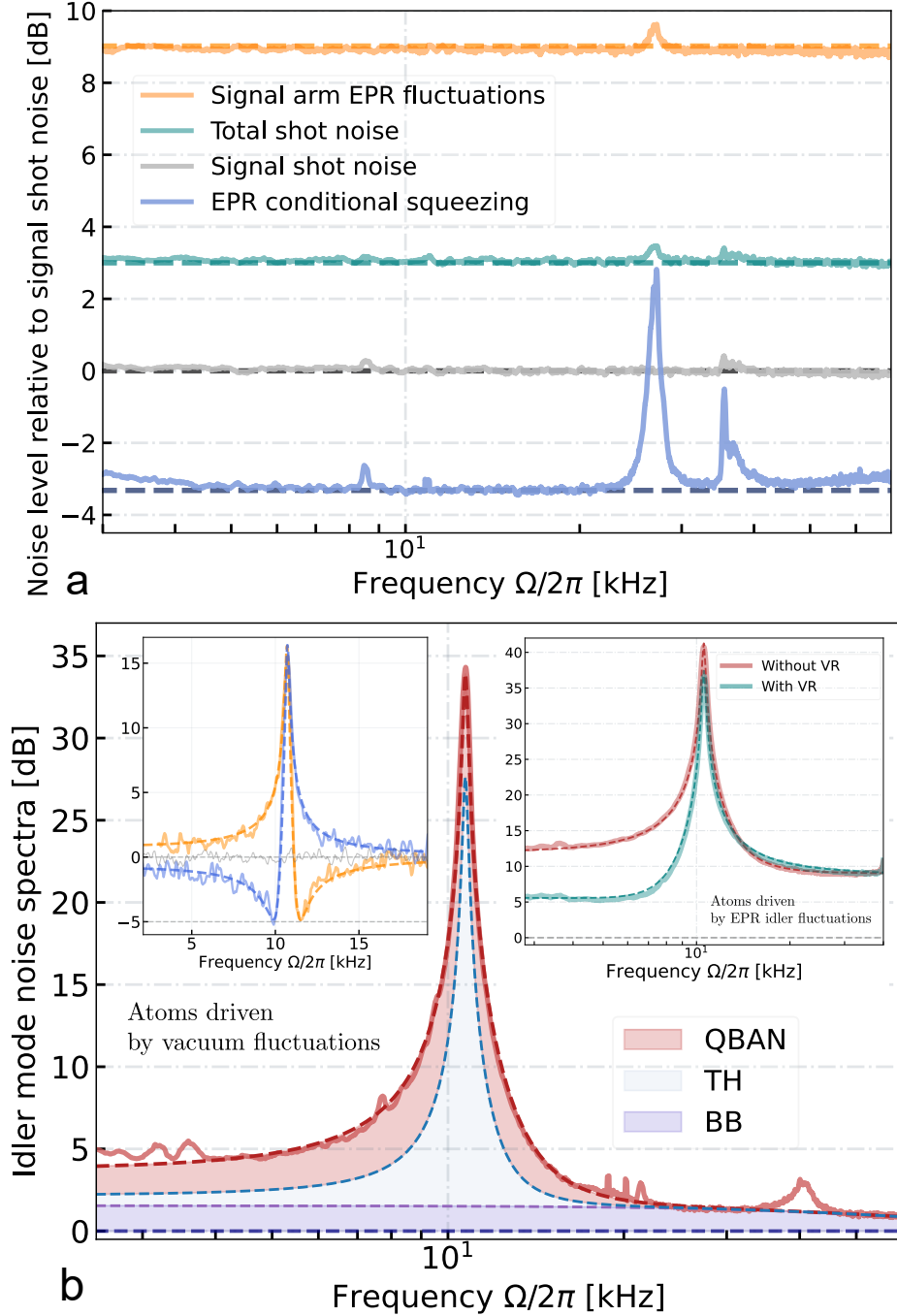
J.J. and Mm.B. developed the atomic spin oscillator setup. T.B.B. designed the two-colour EPR source and built it together with V.N. and A.G.. V.N., J.J., T.B.B., A.G. and Mm.B. performed the data acquisition. E.Z., V.N., J.J. and A.G. developed the analytical model. J.J. and V.N. performed the data analysis. Mk.B. fabricated the caesium cell. J.H.M. contributed with valuable discussions. T.B.B. led the experimental work. V.N., J.J., T.B.B. and A.G. contributed equally to this work. E.S.P. conceived and led the project. All authors contributed to writing the paper.

AUTHOR INFORMATION

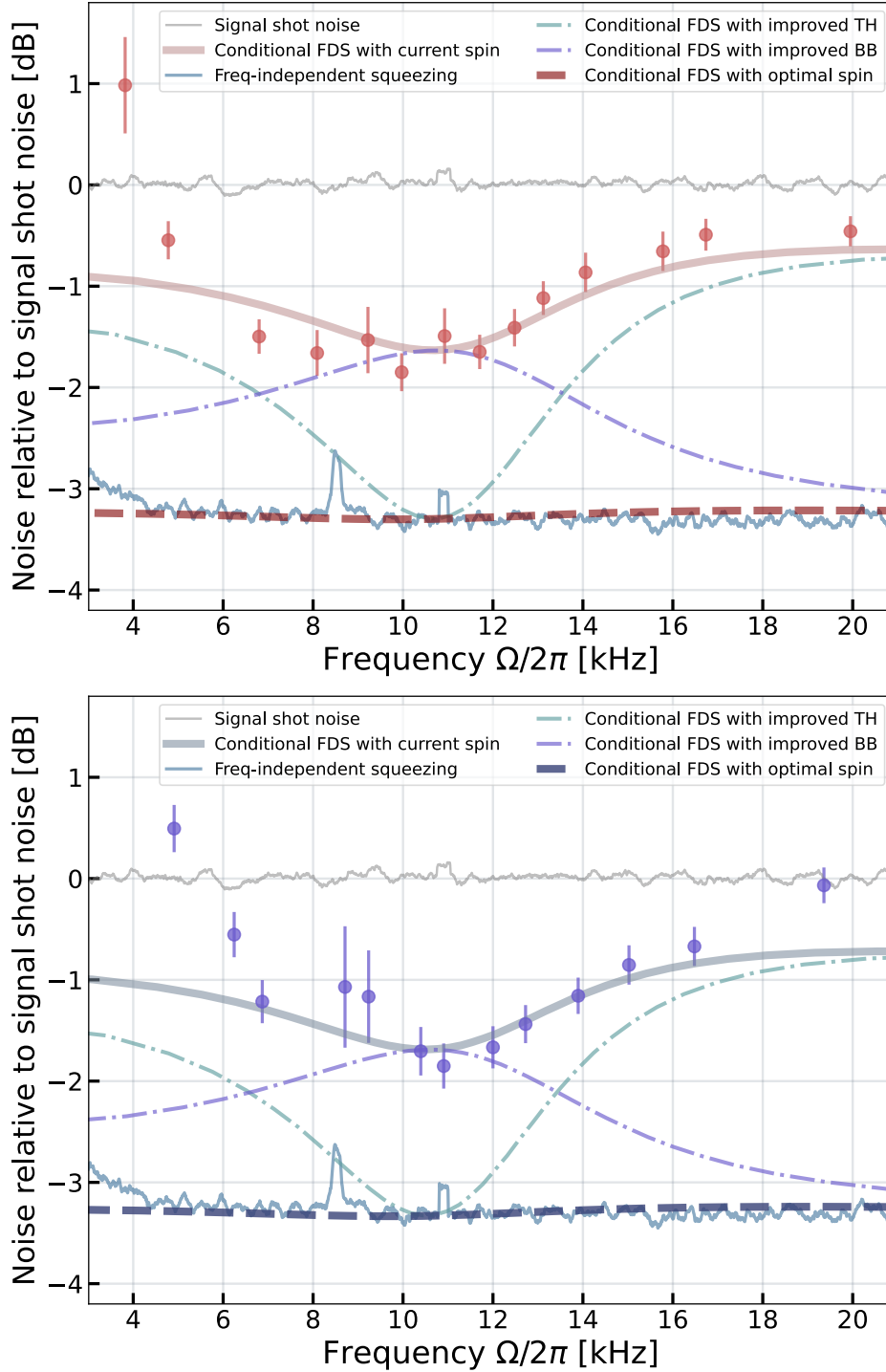
The authors declare no competing financial interests. Correspondence and requests for materials should be addressed to polzik@nbi.ku.dk.



Extended Data Fig. 1. **Experimental Setup Main Components.** The experimental setup includes two lasers: a 1064 nm continuous-wave (CW) laser and a tunable CW Ti:Sapphire laser at 852 nm. The two-colour Einstein-Podolsky-Rosen (EPR) state setup involves two nonlinear optical interactions: sum-frequency generation (SFG) and a non-degenerate optical parametric oscillator (NOPO). The 1064 nm and the 852 nm laser produce the SFG light in a nonlinear crystal, which serves as the pump for the NOPO at with pump phase θ_p . The NOPO generates the EPR state at 1064 nm (signal) and 852 nm (idler), represented by dashed lines. The signal and idler modes are separated by a dichroic mirror. The signal is directed to balanced homodyne detection (HDs) with local oscillator phase θ_s , while the idler is mixed with the probe beam at a polarizing beam splitter (PBS) with relative phase ϕ_i and propagates in free space (~ 10 m) to the atomic oscillator setup. The probe-idler spatial profile is modified to a square top-hat beam by a top-hat shaper (THS) before being sent to the caesium (Cs) vapour cell. The cell is placed inside a magnetic shield with a set of coils controlling the bias magnetic field. The optical pump system prepares the spin ensemble in a highly polarized state. After interaction, the idler quantum state is sent to polarization homodyne detection (HDi) where a quarter-wave plate (QWP) and half-wave plate (HWP) determine the phase shift $\delta\theta_i$. A portion of the 1064 nm laser is frequency-shifted by 3 MHz to produce the coherent-lock field (CLF) beam injected to the NOPO with phase θ_c , which provides the phase reference for the detection system and feedback control of the detected quadratures. The fields for the local oscillators LOs and LOi are produced by the 1064 nm and 852 nm lasers, respectively. Each LO is filtered by a mode-cleaner cavity (not shown). Both photocurrents from the homodyne detectors are sent to a data acquisition (DAQ) system for recording and later post-processing. The quadrature correlations at specific sideband frequencies for different set phases ($\phi_i + \delta\theta_i, \theta_s$) are used to demonstrate the frequency-dependent conditional squeezing. The phases ϕ_i and θ_s are actively stabilized to fix the quadrature detection in relation to the pump phase θ_p .



Extended Data Fig. 2. **Calibration of the hybrid quantum system. a. Quantum noise of light modes in the absence of the atomic spin oscillator.** Teal trace – total shot noise of the signal and idler. Gray trace – shot noise of the signal. Blue trace shows 3.2 dB of conditional, frequency-independent EPR squeezing. It corresponds to $\simeq 6$ dB of entanglement of the EPR state when normalized to the total shot noise of the signal and idler modes (teal trace). Orange trace – signal-arm EPR fluctuations. **b. Idler arm noise spectra in the presence of the atomic spin oscillator.** Main panel: Atoms driven by vacuum fluctuations; the reconstructed quantum-backaction noise (QBAN, red area), the decoherence-associated spin thermal (TH, light-blue area) and broadband noise (BB, purple area) are shown. Left inset: Ponderomotive squeezing of light by atoms observed for two different idler detection angles $\delta\theta_i$. Right inset: Atoms driven by EPR fluctuations; with (teal) and without (red) the virtual rigidity effect. Dashed curves are theoretical fits (see Methods for details). All traces are normalized to the idler shot noise.



Extended Data Fig. 3. **Demonstration of overall quantum noise reduction with potential improvements to the spin oscillator.** Red (positive mass) and blue (negative mass) points show the measured minimal conditional squeezing at each signal phase, along with the overall modelled quantum noise reduction based on the calibrated parameters of the current spin system. The discrepancy between theoretical predictions and experimental data at frequencies below 5 kHz is attributed to residual laser amplitude noise. Estimated conditional squeezing level are also presented for two scenarios: when the atomic thermal (TH) occupation is reduced by a factor of 3 (purple curve) and when the atomic broadband (BB) readout rate is reduced by a factor of 6 (teal curve) relative to current conditions. With both noise sources reduced, the optimal spin system generates the conditional frequency-dependent squeezing (FDS) (red/blue dashed line), limited only by the frequency-independent level of squeezing of light (light blue trace).

Parameter	Symbol	Value
Hybrid system & detection		
Two-mode squeezing factor	r	1.42 1.42 1.31
Propagation efficiency before atoms	$\eta_{i,\text{in}}$	0.89
Overall efficiency after atoms	$\eta_{i,\text{out}}$	0.90
Signal-arm net efficiency (propagation & detection)	η_s	0.92
Idler-arm net efficiency (propagation & detection)	$\eta_i (= \eta_{i,\text{out}}\eta_{i,\text{in}})$	0.8
QWP phase	$\delta\theta_i$	$0^\circ, 42^\circ$
Signal LO power		1 mW
Idler LO power		1 mW
Atomic spin oscillator		
Effective spin oscillator mass		p n p
Larmor frequency	$\Omega_a/2\pi$	10.7 10.5 54 kHz
Spin readout rate	$\Gamma_a/2\pi$	9.3 9.5 8.5 kHz
Spin decoherence rate	$\gamma_a/2\pi$	240 240 200 Hz
Effective spin thermal occupation	n_a	3.5 3.4 4.0
Broadband noise in SN unit at Ω_a		1.8 1.9 1.3 dB
Spin Broadband readout rate	$\Gamma_{bb}/2\pi$	140 130 5 kHz
Spin Broadband decoherence rate	$\gamma_{bb}/2\pi$	190 190 190 kHz
Effective spin broadband occupation	n_{bb}	3.5 3.4 4.0
Probe field detuning	$\Delta_a/2\pi$	1.6 GHz
Probe input polarization	α	45°
Spin polarization		82%

Table I. Summary of notations and experimental parameters for the hybrid quantum system. p | n stands for the positive/negative-mass configuration. The values are estimated by χ^2 fits of the calibration data.

Supplementary Material for “Hybrid quantum network for sensing in the acoustic frequency range”

Valeriy Novikov,^{1,2,*} Jun Jia,^{1,*} Túlio Brito Brasil,^{1,*} Andrea Grimaldi,^{1,*} Maimouna Bocoum,^{3,1} Mikhail Balabas,¹ Jörg Helge Müller,¹ Emil Zeuthen,¹ and Eugene Simon Polzik¹

¹*Niels Bohr Institute, University of Copenhagen,
Blegdamsvej 17, DK-2100 Copenhagen Ø, Denmark*

²*Russian Quantum Center, Skolkovo, Moscow, Russia*

³*ESPCI Paris, PSL University, CNRS, Institut Langevin, Paris 75005, France*

(Dated: December 17, 2024)

In this supplementary material, we detail the theoretical foundations of our work. Specifically, we develop the theory of frequency-dependent conditional squeezing enabled by an atomic spin oscillator and entangled light source using various quantum noise engineering approaches. Additionally, we define the (optimal) Wiener filter for inferring conditional squeezing and outline our practical implementation of the filter. Finally, based on the calibration of the hybrid quantum network performance, we assess the limitations of the current hybrid setup and propose strategies for future improvement.

CONTENTS

I. Theoretical model	2
A. Spin oscillator in the virtual-rigidity configuration	2
B. EPR light source	3
C. Wiener filter	3
1. Atomic spin oscillator without virtual rigidity	3
2. Atomic spin ensemble with virtual rigidity	4
D. Realistic Model of the Atomic Spin Oscillator	5
1. Spin oscillator thermal and broadband noise	5
2. Optical losses	5
3. Realistic model without virtual rigidity	6
4. Realistic model with virtual rigidity	7
II. Data processing	7
A. Wiener filter implementation	7
B. Expected broadband noise reduction with reduced imperfections	9
III. Comparison of the spin system and a filter cavity	9
References	10

* These authors contributed equally

I. THEORETICAL MODEL

In this section, we present the theoretical model used to analyse the experimental data and extract essential parameters for our system. The main results are reported in the Methods; here we present their detailed derivations.

A. Spin oscillator in the virtual-rigidity configuration

The so-called virtual-rigidity configuration is obtained by inserting a quarter-wave plate before the idler homodyne detector in order to generate a phase shift $\delta\theta_i \neq 0$, see Extended Data Fig. 1. In this case, the encoding phase changes to $\phi_i = -\delta\theta_i$, and the Stokes operators become

$$\hat{S}_3^{\text{in}}\sqrt{2}/\alpha_{pr} = -\hat{p}_i \sin(\delta\theta_i) + \hat{x}_i \cos(\delta\theta_i), \quad (\text{S1a})$$

$$\hat{S}_2^{\text{in}}\sqrt{2}/\alpha_{pr} = \hat{p}_i \cos(\delta\theta_i) + \hat{x}_i \sin(\delta\theta_i). \quad (\text{S1b})$$

The backaction on the atomic spin oscillator, driven by \hat{S}_3^{in} , is now defined by a combination of the phase and amplitude quadratures of the idler. The second effect of the quarter-wave plate is the change of the detected quadrature, which becomes proportional to a linear combination of \hat{S}_2 and \hat{S}_3 ,

$$\hat{q}_i(\delta\theta_i) = \frac{\sqrt{2}}{\alpha_{pr}} \left(\hat{S}_2 \cos(\delta\theta_i) + \hat{S}_3 \sin(\delta\theta_i) \right). \quad (\text{S2})$$

Applying Eqs. (S1) to the detected quadrature Eq. (S2) and using Eq. (1) of the main text, we can rewrite the idler photocurrent as a function of the idler canonical quadratures:

$$\hat{q}_i(\delta\theta_i) = \hat{p}_i + \left(\mathcal{K}_a(\Omega) \hat{a}_i^{\pi/2 - \delta\theta_i} + \hat{N}_a(\Omega) \right) \cos(\delta\theta_i), \quad (\text{S3})$$

where $\hat{a}_i^{\pi/2 - \delta\theta_i} = -\hat{p}_i \sin(\delta\theta_i) + \hat{x}_i \cos(\delta\theta_i)$, is a generic input quadrature defined by the encoding phase $\phi_i = -\delta\theta_i$. According to Ref. [1], this equation describes an oscillator with an effective read-out rate Γ_a^{eff} and an effective resonance frequency Ω_a^{eff} ; in terms of the quantities used in the present work, we obtain

$$\Gamma_a^{\text{eff}} = \Gamma_a \frac{\cos(\delta\theta_i)}{\sqrt{1 - \frac{\Gamma_a}{2\Omega_a} \sin(2\delta\theta_i)}}, \quad (\text{S4})$$

$$\Omega_a^{\text{eff}} = \Omega_a \sqrt{1 - \frac{\Gamma_a}{2\Omega_a} \sin(2\delta\theta_i)}. \quad (\text{S5})$$

Equation (S3) can be rewritten using Eqs. (S4) and (S5) as the detected quadrature from an effective oscillator

$$\hat{q}_i(\delta\theta_i) = g_{\text{VR}}(\Omega) [\hat{p}_i + \mathcal{K}_a^{\text{eff}}(\Omega) \hat{x}_i + \hat{N}_a^{\text{eff}}(\Omega)], \quad (\text{S6})$$

scaled by the factor

$$g_{\text{VR}}(\Omega) \equiv 1 + \mathcal{K}_a(\Omega, \Omega_a, \Gamma_a) \frac{\sin(2\delta\theta_i)}{2}, \quad (\text{S7})$$

where the effective backaction contribution is governed by

$$\mathcal{K}_a^{\text{eff}}(\Omega) \equiv \mathcal{K}_a(\Omega, \Omega_a^{\text{eff}}, \Gamma_a^{\text{eff}}) = \frac{\Gamma_a^{\text{eff}} \Omega_a^{\text{eff}}}{(\Omega_a^{\text{eff}})^2 - \Omega^2 - i\gamma_a \Omega + \gamma_a^2/4}, \quad (\text{S8})$$

and the effective atomic noise associated with a finite decay is

$$\hat{N}_a^{\text{eff}}(\Omega) \equiv \frac{\hat{N}_a(\Omega) \cos(\delta\theta_i)}{g_{\text{VR}}(\Omega)}. \quad (\text{S9})$$

B. EPR light source

Here we introduce the formal definitions for noise spectral densities employed in this work. We also specify the spectral densities characterizing the EPR source as well as extraneous sources of vacuum noise.

The symmetrized cross-correlation spectrum $S_{a,b}$ of two operators a and b is evaluated via

$$S_{a,b}(\Omega)\delta(\Omega - \Omega') = \frac{1}{2} \left\langle \hat{a}(\Omega)\hat{b}^\dagger(\Omega') + \hat{b}^\dagger(\Omega')\hat{a}(\Omega) \right\rangle, \quad (\text{S10})$$

which is generally complex-valued and obeys $S_{b,a}(\Omega) = S_{a,b}^*(\Omega)$; $\delta(\Omega - \Omega')$ is the Dirac delta function. The auto-correlation of an operator \hat{a} amounts to the special case $\hat{a} = \hat{b}$ of Eq. (S10),

$$S_a(\Omega) \equiv S_{a,a}(\Omega). \quad (\text{S11})$$

According to the commutation relations $[\hat{x}_i(t), \hat{p}_i(t')] = [\hat{x}_s(t), \hat{p}_s(t')] = i\delta(t - t')$, the symmetrised power spectral density for vacuum fields are

$$S_{SN} \equiv S_{v_x} = S_{v_p} = \frac{1}{2}, \quad (\text{S12})$$

$$S_{v_x, v_p} = 0. \quad (\text{S13})$$

With this convention, the following spectral densities characterise the entangled outputs of the EPR source

$$S_{x_s} = S_{p_s} = S_{x_i} = S_{p_i} = \frac{\cosh(2r)}{2}, \quad (\text{S14})$$

$$S_{x_s, x_i} = -S_{p_s, p_i} = \frac{\sinh(2r)}{2}; \quad (\text{S15})$$

all other cross-spectral densities involving those operators are zero.

C. Wiener filter

As already mentioned in Methods, squeezing in the joint conditional signal $Q_{s|i} = q_s(\theta_s) + gq_i(\theta_i)$ is optimized by varying $g(\Omega)$ using the Wiener filter theory. In the subsequent subsections we evaluate the squeezing performance on the basis of the model.

For convenience, we restate the expression for the optimal filter and the resulting conditional squeezing here (also presented in Methods). The optimal gain is given by

$$g(\Omega, \theta_s, \delta\theta_i) = -\frac{S_{q_s, q_i}(\Omega, \theta_s, \delta\theta_i)}{S_{q_i}(\Omega, \delta\theta_i)}, \quad (\text{S16})$$

which leads to the power spectral density of the optimised signal

$$S_{Q_{s|i}}(\Omega, \theta_s, \delta\theta_i) = S_{q_s}(\Omega, \theta_s) - \frac{|S_{q_s, q_i}(\Omega, \theta_s, \delta\theta_i)|^2}{S_{q_i}(\Omega, \delta\theta_i)}. \quad (\text{S17})$$

1. Atomic spin oscillator without virtual rigidity

In the case $\delta\theta_i = 0$, we are measuring the atomic spin oscillator without the quarter wave plate in the polarimetric homodyne detector. This configuration is described by

$$\hat{q}_s(\theta_s) = \hat{x}_s \sin(\theta_s) + \hat{p}_s \cos(\theta_s), \quad (\text{S18a})$$

$$\hat{q}_i(\delta\theta_i = 0) = \hat{p}_i + \mathcal{K}_a \hat{x}_i + \hat{N}(\Omega). \quad (\text{S18b})$$

By using Eqs. (S18) and noting that the only non-zero cross-correlations are given by Eqs. (S15), we find that

$$S_{q_s, q_i}(\Omega) = \frac{\sinh(2r)}{2} [-\cos(\theta_s) + \sin(\theta_s)\mathcal{K}_a^*(\Omega)]. \quad (\text{S19})$$

The spectral density of the atomic spin oscillator signal is given by

$$\begin{aligned} S_{q_i}(\Omega) &= S_{p_i} + |\mathcal{K}_a(\Omega)|^2 S_{x_i} + S_N(\Omega) \\ &= \frac{\cosh(2r)}{2} (1 + |\mathcal{K}_a(\Omega)|^2) + S_N(\Omega), \end{aligned} \quad (\text{S20})$$

where S_N is the spectrum of the uncorrelated noise, which will be described in Section ID.

We can use Eq. (S16) to calculate the Wiener filter

$$g(\Omega, \theta_s, \delta\theta_i = 0) = \tanh(2r) \frac{\cos(\theta_s) - \sin(\theta_s)\mathcal{K}_a^*(\Omega)}{1 + |\mathcal{K}_a(\Omega)|^2 + \frac{2S_N(\Omega)}{\cosh(2r)}}, \quad (\text{S21})$$

and Eq. (S17) to estimate the conditional noise spectral density of the combined system as

$$\frac{S_{Q_{s|i}}(\Omega, \theta_s, \delta\theta_i = 0)}{S_{SN}} = \cosh(2r) - \tanh(2r) \sinh(2r) \frac{|\cos(\theta_s) - \sin(\theta_s)\mathcal{K}_a(\Omega)|^2}{1 + |\mathcal{K}_a(\Omega)|^2 + \frac{2S_N(\Omega)}{\cosh(2r)}}, \quad (\text{S22})$$

where we have renormalised by the shot-noise spectral density of the idler arm $S_{SN} = 1/2$.

2. Atomic spin ensemble with virtual rigidity

The configuration $\delta\theta_i \neq 0$ corresponds to using the quarter wave plate in the polarimetric homodyne detection to manipulate the input-output relationship of the atomic spin oscillator. The normalized signal and idler photocurrents are

$$\hat{q}_s(\theta_s) = \hat{x}_s \sin(\theta_s) + \hat{p}_s \cos(\theta_s), \quad (\text{S23})$$

$$\hat{q}_i(\delta\theta_i) = \hat{p}_i + \mathcal{K}_a \hat{a}_i^{\pi/2 - \delta\theta_i} \cos(\delta\theta_i) + \hat{N}(\Omega) \cos(\delta\theta_i), \quad (\text{S24})$$

where $\hat{a}_i^{\pi/2 - \delta\theta_i} = \hat{x}_i \cos(\delta\theta_i) + \hat{p}_i \sin(\delta\theta_i)$. As we described in Section IA, we can rewrite the idler quadrature

$$\hat{q}_i(\delta\theta_i) = g_{VR}(\Omega, \delta\theta_i) \left[\hat{p}_i + \mathcal{K}_a^{\text{eff}} \hat{x}_i + \hat{N}_a^{\text{eff}} \right] = g_{VR}(\Omega, \delta\theta_i) \hat{q}_i^{\text{eff}}, \quad (\text{S25})$$

which corresponds to the response of an effective oscillator.

The correlation between the photocurrents S_{q_s, q_i} can be evaluated by noting that

$$\hat{q}_s \hat{q}_i^\dagger = g_{VR}^* (\hat{q}_s (\hat{q}_i^{\text{eff}})^\dagger). \quad (\text{S26})$$

Based on this observation, we can re-adapt the result of Eq. (S19) and calculate the cross-spectral density by replacing $\mathcal{K}_a \rightarrow \mathcal{K}_a^{\text{eff}}$

$$S_{q_s q_i} = g_{VR}^*(\Omega) \frac{\sinh(2r)}{2} (-\cos(\theta_s) + \sin(\theta_s) [\mathcal{K}_a^{\text{eff}}(\Omega)]^*). \quad (\text{S27})$$

Based on the same observation, the power spectral density of the atomic spin signal can be calculated as

$$S_{q_i}(\delta\theta_i) = |g_{VR}(\Omega)|^2 \left[\frac{\cosh(2r)}{2} (1 + |\mathcal{K}_a^{\text{eff}}(\Omega)|^2) + S_N^{\text{eff}}(\Omega) \right]. \quad (\text{S28})$$

By combining the two equations, we can estimate the optimal gain

$$g(\Omega, \theta_s, \delta\theta_i) = g_{VR}^{-1}(\Omega) \tanh(2r) \frac{\cos(\theta_s) - \sin(\theta_s) [\mathcal{K}_a^{\text{eff}}(\Omega)]^*}{1 + |\mathcal{K}_a^{\text{eff}}(\Omega)|^2 + \frac{2S_N^{\text{eff}}(\Omega)}{\cosh(2r)}}, \quad (\text{S29})$$

and the power spectral density of the optimised signal in the units of shot noise is

$$\frac{S_{Q_{s|i}}(\Omega, \theta_s, \delta\theta_i)}{S_{SN}} = \cosh(2r) - \tanh(2r) \sinh(2r) \frac{|\cos(\theta_s) - \sin(\theta_s)\mathcal{K}_a^{\text{eff}}(\Omega)|^2}{1 + |\mathcal{K}_a^{\text{eff}}(\Omega)|^2 + \frac{2S_N^{\text{eff}}(\Omega)}{\cosh(2r)}}, \quad (\text{S30})$$

where the normalisation factor $g_{VR}(\Omega)$ is absorbed by the optimal gain $g(\Omega, \theta_s, \delta\theta_i)$ and the dependency on $\delta\theta_i$ is contained in the effective quantities $\mathcal{K}_a^{\text{eff}}$ and S_N^{eff} .

D. Realistic Model of the Atomic Spin Oscillator

1. Spin oscillator thermal and broadband noise

In the calculation presented until now, we have collected the uncorrelated noise contribution in the operator $\hat{N}_a(\Omega)$. Here, we provide the explicit expression and derive its noise spectral density $S_N(\Omega)$. During the light-spin interaction, the spin oscillator experiences dissipation, which can be described using the quantum Langevin methods, as outlined in Refs. [2, 3]. The dissipation leads to the noise which has two main contributions: (1) The thermal noise, associated with a finite decay $\gamma_a > 0$, which is primarily due to the spontaneous emission of the probe photons, and (2) the broadband noise generated by imperfect coupling between the idler beam and the atomic spins moving within the vapour cell. The thermal noise is given by $\mathcal{K}_a(\Omega)\hat{F}_a$, while the broadband noise is given by another frequency-dependent contribution $\mathcal{K}_{bb}(\Omega)\hat{F}_{bb}$. We those two contributions the equation for the Stokes operator reads:

$$\begin{aligned}\hat{S}_3^{\text{out}} &= \hat{S}_3^{\text{in}} + \mathcal{K}_a\hat{S}_2^{\text{in}} + \mathcal{N}_a \\ &= \hat{S}_3^{\text{in}} + \mathcal{K}_a\hat{S}_2^{\text{in}} + \left(\mathcal{K}_{th}(\Omega)\hat{F}_a + \mathcal{K}_{bb}(\Omega)\hat{F}_{bb}\right) \frac{\alpha_{pr}}{\sqrt{2}}.\end{aligned}\quad (\text{S31})$$

where

$$\mathcal{K}_{th}(\Omega) = \frac{\sqrt{2\gamma_a\Gamma_a}\Omega_a}{\Omega_a^2 - \Omega^2 - i\gamma_a\Omega + \gamma_a^2/4}, \quad (\text{S32a})$$

$$\mathcal{K}_{bb}(\Omega) = \frac{\sqrt{2\gamma_{bb}\Gamma_{bb}}\Omega_a}{\Omega_a^2 - \Omega^2 - i\gamma_{bb}\Omega + \gamma_{bb}^2/4}, \quad (\text{S32b})$$

where γ_a and Γ_a are the decay rate and the readout rate for the atomic narrowband response, and γ_{bb} and Γ_{bb} are the decay rate and the readout rate for the broadband dynamics. In our experiment, where $|\Omega_a| \gg \gamma_a, \Gamma_{bb}$, the thermal dynamics of the two transverse collective spin components contribute approximately equally to the output light, resulting in the factor of $\sqrt{2}$ in $\mathcal{K}_{th}(\Omega)$ and $\mathcal{K}_{bb}(\Omega)$. The spectrum of coupling to the thermal reservoirs, whose Langevin operators obey $[\hat{F}_a^x(t), \hat{F}_a^p(t')] = [\hat{F}_{bb}^x(t), \hat{F}_{bb}^p(t')] = i\delta(t-t')$, is characterised by the effective thermal occupation numbers n_{th} and n_{bb} , [2, 3]

$$S_{F_a} = n_{th} + \frac{1}{2}, \quad S_{F_{bb}} = n_{bb} + \frac{1}{2}. \quad (\text{S33})$$

The effective thermal occupation is linked to the internal spin state of the atomic ensemble. The purity of a coherent spin state, characterized by its spin polarization, can be quantified by using the magneto-optical resonance method (MORS)[4]. The experimental thermal occupation number is typically larger than the value estimated from the spin polarization. This is due to the influence of the classical probe intensity noise and environmental disturbances, as discussed in Ref. [3]. For the data analysis, the effective thermal occupations of the narrowband n_{th} and broadband n_{bb} modes are taken to be the same.

2. Optical losses

The losses in the idler arm have to be divided between the input efficiency $\eta_{i,\text{in}}$ and the output efficiency $\eta_{i,\text{out}}$, which correspond to the optical losses acquired before and after the interaction with the atomic spin oscillator, respectively. The losses modify the input Stokes quadratures as

$$\hat{S}_3^{\text{in}}\sqrt{2}/\alpha_{pr} = \sqrt{\eta_{i,\text{in}}}\hat{q}_i + \sqrt{1-\eta_{i,\text{in}}}\hat{v}_{i,\text{in}}(\phi_i), \quad (\text{S34})$$

$$\hat{S}_2^{\text{in}}\sqrt{2}/\alpha_{pr} = \sqrt{\eta_{i,\text{in}}}\hat{q}_{i+\pi/2} + \sqrt{1-\eta_{i,\text{in}}}\hat{v}_{i,\text{in}}(\phi_i + \pi/2), \quad (\text{S35})$$

where, $\hat{v}_{i,\text{in}}(\phi_i)$ and $\hat{v}_{i,\text{in}}(\phi_i + \pi/2)$ are the quadratures of the vacuum entering before the interaction with the atomic spin oscillator. The output losses correspond to injection of another vacuum state $\hat{v}_{i,\text{out}}^0$

$$\hat{Q}_i(\delta\theta_i) = \sqrt{\eta_{i,\text{out}}}\left(\hat{S}_3\cos(\delta\theta_i) + \hat{S}_2\sin(\delta\theta_i)\right) + \sqrt{1-\eta_{i,\text{out}}}\hat{v}_{i,\text{out}}^0. \quad (\text{S36})$$

The final expression for the photocurrent is quite crowded, and for the sake of simplicity, we will derive the results first without the quarter wave plate, $\delta\theta_i = 0$, and then in the case when it is included, $\delta\theta_i \neq 0$.

3. Realistic model without virtual rigidity

In the absence of virtual rigidity effect, $\delta\theta_i = 0$, the input idler phase $\phi_i = 0$, and the idler photocurrent is

$$\hat{q}_i(\delta\theta_i = 0) = \sqrt{\eta_{i,\text{out}}} \left[\sqrt{\eta_{i,\text{in}}} (\hat{p}_i - \mathcal{K}_a \hat{x}_i) + \sqrt{1 - \eta_{i,\text{in}}} \left(\hat{v}_{i,\text{in}}^0 - \mathcal{K}_a \hat{v}_{i,\text{in}}^{\pi/2} \right) + \mathcal{K}_{th}(\Omega) \hat{F}_a + \mathcal{K}_{bb}(\Omega) \hat{F}_{bb} + \frac{\sqrt{1 - \eta_{i,\text{out}}}}{\sqrt{\eta_{i,\text{out}}}} \hat{v}_{i,\text{out}}^0 \right], \quad (\text{S37})$$

where we can identify four new contributions to the final photocurrent:

$$\hat{\Sigma}_{i,\text{in}} = \sqrt{1 - \eta_{i,\text{in}}} \left(\hat{v}_{i,\text{in}}^0 - \mathcal{K}_a \hat{v}_{i,\text{in}}^{\pi/2} \right), \quad (\text{S38})$$

is the response of the atomic spin oscillator to the vacuum appearing due to the sub-optimal coupling;

$$\hat{\Sigma}_{\text{th}} = \mathcal{K}_{th}(\Omega) \hat{F}_a, \quad (\text{S39})$$

is the thermal noise;

$$\hat{\Sigma}_{\text{bb}} = \mathcal{K}_{bb}(\Omega) \hat{F}_{bb}, \quad (\text{S40})$$

is the broadband noise; and

$$\hat{\Sigma}_{i,\text{out}} = \hat{v}_{i,\text{out}}^0 \sqrt{1 - \eta_{i,\text{out}}} / \sqrt{\eta_{i,\text{out}}}, \quad (\text{S41})$$

is the effect of imperfect readout efficiency.

The new terms will affect the power spectral density of the idler signal by adding new contributions

$$\Lambda_{\text{in}}(\Omega) \equiv S_{\Sigma_{i,\text{in}}}(\Omega) = \frac{1 - \eta_{i,\text{in}}}{2} \left(1 + |\mathcal{K}_a(\Omega)|^2 \right), \quad (\text{S42a})$$

$$\Lambda_{\text{out}}(\Omega) \equiv S_{\Sigma_{i,\text{out}}}(\Omega) = \frac{1 - \eta_{i,\text{out}}}{2\eta_{i,\text{out}}}, \quad (\text{S42b})$$

$$S_{\text{th}}(\Omega) \equiv S_{\Sigma_{\text{th}}}(\Omega) = |\mathcal{K}_{th}(\Omega)|^2 (1/2 + n_{\text{th}}), \quad (\text{S42c})$$

$$S_{\text{bb}}(\Omega) \equiv S_{\Sigma_{\text{bb}}}(\Omega) = |\mathcal{K}_{bb}(\Omega)|^2 (1/2 + n_{\text{bb}}), \quad (\text{S42d})$$

which add up to

$$S_{q_i} = \eta_{i,\text{out}} \left[\frac{\cosh(2r)\eta_{i,\text{in}}}{2} \left(1 + |\mathcal{K}_a|^2 \right) + \frac{1 - \eta_{i,\text{in}}}{2} \left(1 + |\mathcal{K}_a|^2 \right) + S_{\Sigma_{\text{th}}} + S_{\Sigma_{\text{bb}}} + \frac{1 - \eta_{i,\text{out}}}{2\eta_{i,\text{out}}} \right]. \quad (\text{S43})$$

The cross-correlation between the photocurrents is affected only by the losses on the idler and the signal, and it is reduced as

$$S_{q_s, q_i} = -\sqrt{\eta_s \eta_{i,\text{out}} \eta_{i,\text{in}}} \frac{\sinh(2r)}{2} (\cos(\theta_s) - \sin(\theta_s) [\mathcal{K}_a(\Omega)]^*), \quad (\text{S44})$$

and the spectrum of the signal photocurrent is

$$S_{q_s} = \eta_s \frac{\cosh(2r)}{2} + \frac{1 - \eta_s}{2}, \quad (\text{S45})$$

The power spectral density of the optimised signal is evaluated using Eq. (S17) as

$$\frac{S_{Q_{s|i}}(\Omega, \theta_s, \delta\theta_i = 0)}{S_{SN}} = 1 - \eta_s + \frac{\eta_s}{\cosh(2r)} \left[\cosh^2(2r) - \frac{\sinh^2(2r) |\cos(\theta_s) - \sin(\theta_s) \mathcal{K}_a|^2}{1 + |\mathcal{K}_a|^2 + 2 \frac{\Lambda_{\text{in}} + \Lambda_{\text{out}} + S_{\text{th}} + S_{\text{bb}}}{\eta_{i,\text{in}} \cosh(2r)}} \right]. \quad (\text{S46})$$

in terms of the quantities (S42), highlighting the contributions of different imperfections (dependencies on Ω are omitted for brevity).

4. Realistic model with virtual rigidity

Even in the realistic model, we can use the virtual rigidity renormalisation, Eq. (S7), to reinterpret the effect of the quarter waveplate as a shift of the resonance frequency, Eq. (S5) and rescaling of the readout rate, Eq. (S4) on the backaction coefficient \mathcal{K}_a . Here, we discuss the effect of the virtual rigidity renormalisation on the thermal noise, the broadband noise and the optical losses. In the virtual rigidity configuration, the idler photocurrent is proportional to:

$$\hat{q}_i(\delta\theta_i) = \sqrt{\eta_{i,\text{out}}}g_{\text{VR}}(\Omega) \left[\sqrt{\eta_{i,\text{in}}}(\hat{p}_i - \mathcal{K}_a^{\text{eff}}(\Omega)\hat{x}_i) + \sqrt{1 - \eta_{i,\text{in}}}(\hat{v}_{i,\text{in}}^0 - \mathcal{K}_a^{\text{eff}}(\Omega)\hat{v}_{i,\text{in}}^{\pi/2}) \right. \\ \left. + \mathcal{K}_{th}^{\text{eff}}(\Omega)\hat{F}_a + \mathcal{K}_{bb}^{\text{eff}}(\Omega)\hat{F}_{bb} + \frac{\sqrt{1 - \eta_{i,\text{out}}}}{\sqrt{\eta_{i,\text{out}}}g_{\text{VR}}(\Omega)}\hat{v}_{i,\text{out}}^0 \right], \quad (\text{S47})$$

where $g_{\text{VR}}(\Omega)$ is the virtual rigidity gain defined in Eq. (S7), $\mathcal{K}_a^{\text{eff}}$ is the effective atomic transfer function defined in Eq. (S8), and $\mathcal{K}_{th}^{\text{eff}}(\Omega)$ and $\mathcal{K}_{bb}^{\text{eff}}(\Omega)$ are the effective transfer functions for the thermal and broadband noise,

$$\mathcal{K}_{th}^{\text{eff}}(\Omega) \equiv \frac{\cos(\delta\theta_i)}{g_{\text{VR}}(\Omega)}\mathcal{K}_{th}(\Omega), \quad (\text{S48})$$

$$\mathcal{K}_{bb}^{\text{eff}}(\Omega) \equiv \frac{\cos(\delta\theta_i)}{g_{\text{VR}}(\Omega)}\mathcal{K}_{bb}(\Omega). \quad (\text{S49})$$

The Eqs. (S47) and (S37) are similar, and are related by the following replacements

$$\mathcal{K}_{th} \rightarrow \mathcal{K}_{th}^{\text{eff}}, \quad (\text{S50})$$

$$\mathcal{K}_{bb} \rightarrow \mathcal{K}_{bb}^{\text{eff}}, \quad (\text{S51})$$

$$\frac{\sqrt{1 - \eta_{i,\text{out}}}}{\sqrt{\eta_{i,\text{out}}}} \rightarrow \frac{\sqrt{1 - \eta_{i,\text{out}}}}{\sqrt{\eta_{i,\text{out}}}g_{\text{VR}}(\Omega)}, \quad (\text{S52})$$

which lead to the effective noise contribution factors [cf. Eqs. (S42)]

$$\Lambda_{\text{in}}^{\text{eff}}(\Omega) = \frac{1 - \eta_{i,\text{in}}}{2}(1 + |\mathcal{K}_a^{\text{eff}}(\Omega)|^2), \quad (\text{S53a})$$

$$\Lambda_{\text{out}}^{\text{eff}}(\Omega) = \frac{1 - \eta_{i,\text{out}}}{2\eta_{i,\text{out}}} \frac{1}{|g_{\text{VR}}(\Omega)|^2}, \quad (\text{S53b})$$

$$S_{\text{th}}^{\text{eff}}(\Omega) = \left| \frac{\cos(\delta\theta_i)\mathcal{K}_{th}(\Omega)}{g_{\text{VR}}(\Omega)} \right|^2 (1/2 + n_{\text{th}}), \quad (\text{S53c})$$

$$S_{\text{bb}}^{\text{eff}}(\Omega) = \left| \frac{\cos(\delta\theta_i)\mathcal{K}_{bb}(\Omega)}{g_{\text{VR}}(\Omega)} \right|^2 (1/2 + n_{\text{bb}}). \quad (\text{S53d})$$

These effective noise contributions are inserted in Eq. (S46)

$$\frac{S_{Q_{s|i}}(\Omega, \theta_s, \delta\theta_i)}{S_{SN}} = 1 - \eta_s + \frac{\eta_s}{\cosh(2r)} \left[\cosh^2(2r) - \frac{\sinh^2(2r) |\cos(\theta_s) - \sin(\theta_s)\mathcal{K}_a^{\text{eff}}|^2}{1 + |\mathcal{K}_a^{\text{eff}}|^2 + 2\frac{\Lambda_{\text{in}}^{\text{eff}} + \Lambda_{\text{out}}^{\text{eff}} + S_{\text{th}}^{\text{eff}} + S_{\text{bb}}^{\text{eff}}}{\eta_{i,\text{in}} \cosh(2r)}} \right], \quad (\text{S54})$$

where, on the right-hand side, the dependency on $\delta\theta_i$ is contained in the effective quantities ('eff') and the dependencies on Ω are omitted for brevity.

II. DATA PROCESSING

A. Wiener filter implementation

In the previous section, we developed the analytical model to predict the noise spectra for joint continuous measurements in the signal and idler channels using the optimal Wiener gain to achieve the maximum conditional squeezing.

This frequency-dependent optimal weighting can be determined experimentally through the cross-correlations between two entangled channels, as discussed in Refs. [5–7]. Here we implement this procedure and present the post-processing method which allows us to infer the optimal conditional squeezing directly using the cross-correlation between the recorded signal and idler time series. This can be contrasted with Wiener-filter protocols for inferring the state of a system coupled to light, which requires a model for the system dynamics and input-output relations [2, 8–10]. Nevertheless, the predicted conditional squeezing—based solely on the cross-correlation between the signal and idler channels—provides a cross-validation method to test the agreement of our theoretical model with the calibrated parameters as discussed in the main text.

The recorded photocurrents from both signal and idler detectors are saved as time series data, as shown in Fig. S1(a). The corresponding power spectral densities (PSD) are calculated using Welch’s method. Additionally, we estimate the complex cross power spectral density (CSD) between the idler and signal time series under the same PSD parameters. This estimated CSD, together with the previously computed idler power spectrum density, is used to design the Wiener filter gain $g(\Omega) = -S_{q_i, q_s}(\Omega)/S_{q_i}(\Omega)$. We then apply this filter gain by convolving it with the idler beam time series, thereby optimally suppressing uncorrelated noise and compensating for the frequency-dependent phase lag arising from the damping of the atomic spin oscillator (highlighted by the imaginary components in royal blue trace). The resulting filtered idler time series represented by the light red curve in Fig. S1(d)] is subsequently combined with the original signal (blue curve) to infer the minimal conditional squeezing level. As shown in Fig. S1(e), the conditional spectrum (the orange curve) is significantly suppressed compared to the original signal’s PSD (the blue curve).

Therefore, beyond the broadband quantum noise reduction achievable when both the measurement rate and complex susceptibility of the spin oscillator are matched with the target sensors, the reported conditional quantum noise reduction of the signal mode at different detection phases—effectively treated as a sensor with purely real frequency response—opens up the potential for achieving broadband quantum noise reduction in other systems, even those without intrinsic damping (such as free-mass gravitational wave detectors).

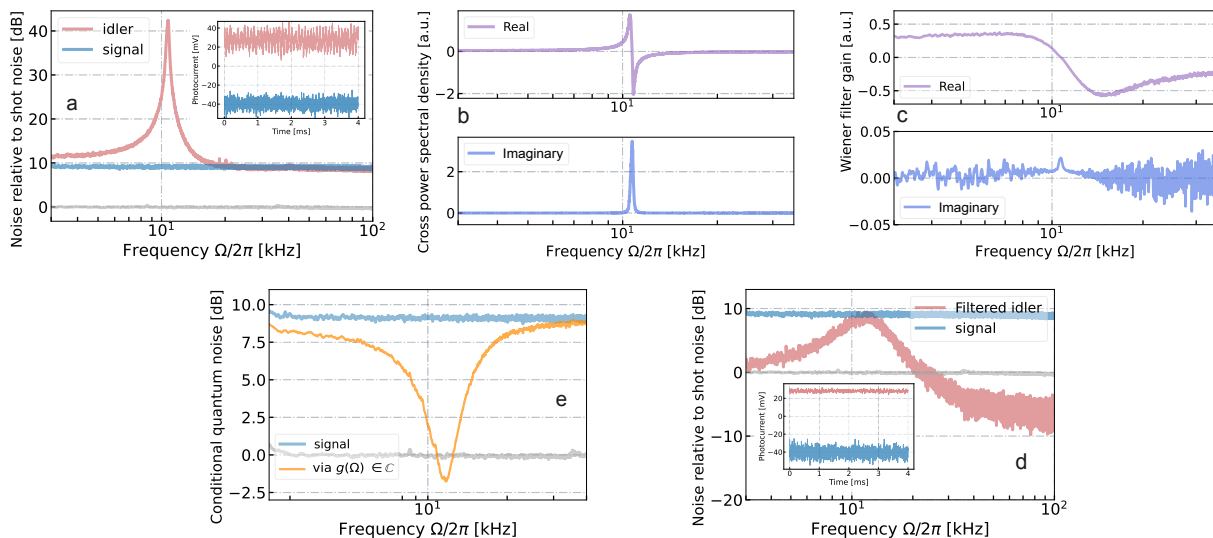


Figure S1. Conditional squeezing by Wiener filtering based on the measured cross-correlation spectrum of entangled channels. The signal analysis is performed with the signal measured at near amplitude quadrature ($\theta_s = 80^\circ$). The spin oscillator is operated in the positive-mass configuration and the idler field is detected at phase quadrature ($\delta\theta_i = 0^\circ$). (a) Recorded photocurrents of the signal (blue curve) and idler (red curve) fields are presented over a 4 ms window out of a total 60 s measurement, along with their power spectral densities estimated via Welch’s method. (b) The time series of the signal and idler are used to calculate the complex cross-power spectral density using Welch’s method, The real (purple curve) and imaginary (blue curve) components are shown. (c) The optimal complex Wiener filter gain $g(\Omega)$ is computed using the estimated cross-power spectral and the idler’s autocorrelation function. (d) The experimentally determined optimal filter gain is applied to the idler data, enabling the estimation of the filtered idler signal (shown by the red trace). (e) The original signal time series and the filtered idler series are combined to estimate the optimal conditional squeezing level (orange curve).

In Fig. S2(a,b,c), we present the minimal conditional, frequency-dependent squeezing for three different signal homodyne phases ($90^\circ, 140^\circ, 180^\circ$), along with their corresponding complex Wiener gains. Furthermore, as illustrated in Fig. S2(d,e,f), activating the virtual rigidity in the idler arm we observe a clear downshift in the frequency associated with the minimal squeezing level compared to the configurations without virtual rigidity for all three phases presented in the Figure. The value of the frequency downshift varies for different signal readout angles, which can be attributed

to a reduced effective atomic readout rate. The effective downshift is accompanied by asymmetric quantum noise reduction. Specifically, above the original Larmor frequency, we observe the enhanced ≈ -2.5 dB conditional squeezing [red curve in Fig. S2(f) compared to Fig. S2(c)].

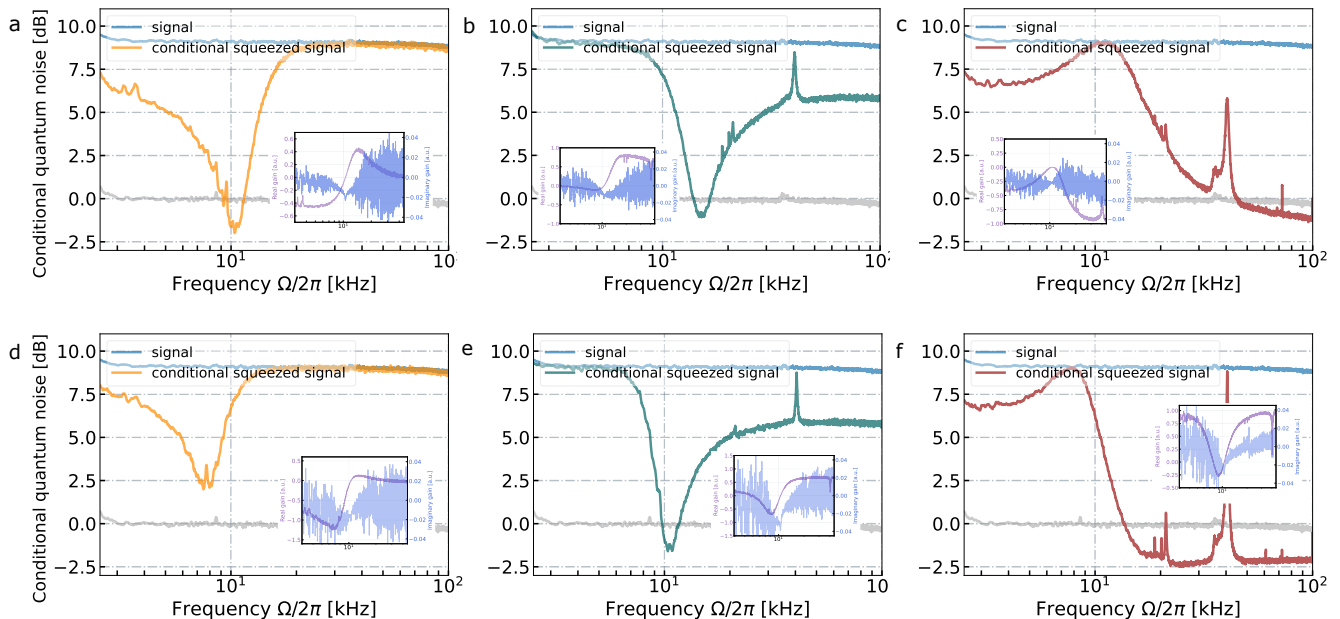


Figure S2. **Conditional squeezing with and without virtual rigidity shift for different signal detection phases θ_s .** The atomic spin oscillator is operated in the negative-mass configuration. (a-c) Conditional squeezing level of the signal beam is estimated using the optimal Wiener gain based on the idler beam measured in the phase quadrature. The signal beam is detected at the phase of 90° (orange), 140° (teal), 180° (red), respectively, each with their corresponding complex Wiener gains [represented by their real (purple) and imaginary (blue) components]. (d-f) Introducing a quarter waveplate enables a virtual frequency downshift, altering the optimal Wiener gain and shifting the minimal conditional squeezing level for each signal detection phase. The minimal quantum noise level remains nearly unchanged for the configuration without virtual rigidity. However, with the virtual rigidity shift applied, the minimal conditional squeezing level exhibits dependence on the Fourier frequency.

B. Expected broadband noise reduction with reduced imperfections

Potential enhancement of the hybrid conditional frequency-dependent squeezing can be achieved by reducing losses and eliminating extra noise. Extended Data Fig. 3 presents the minimal noise spectrum obtained from joint measurements optimized across various signal homodyne phases (red data points). Our theoretical model with calibrated parameters from the current experiment fits the experimental data well. Using this model, we can predict the performance improvements achievable by reducing various imperfections. A reduction in the effective thermal occupation number from its initial value of $n_{th} \approx 3.5$ by a factor of 3 primarily reduces quantum noise around the Larmor frequency (purple curve). This improvement can be realized through enhanced optical pumping and further suppression of classical noise sources, including those from the probe laser and the environment. Additionally, decreasing the atomic broadband noise readout rate by a factor of 6 can be achieved by enlarging the filling factor of the top-hat beam that reduces the quantum noise both above and below the Larmor frequency (green curve). Combining these improvements, we anticipate achieving the 3 dB conditional frequency-dependent squeezing achieved with the atomic spin oscillator limited only by the degree of squeezing of light.

III. COMPARISON OF THE SPIN SYSTEM AND A FILTER CAVITY

Consider a Fabry-Pérot filter cavity with a distance L_f between the two mirrors. In the low-intracavity-loss approximation, the quadrature phase shift of a detuned filter cavity can be approximated by [11–13]

$$\Phi_f(\Omega) \approx \arctan \left[\frac{2\delta_f\gamma_f}{\gamma_f^2 - \delta_f^2 + \Omega^2} \right], \quad (\text{S55})$$

where Ω is the sideband frequency, δ_f is the filter cavity detuning from the field carrier frequency and γ_f is the filter cavity bandwidth.

As an example, we consider a filter cavity with finesse $\mathcal{F} = 6000$, a value similar to that reported in Ref. [14]. To compare the transformation of the squeezed state by a filter cavity and by our system, we fit the readout angle of the conditional frequency-dependent noise spectra shown in Fig. 3 of the main text with Eq. (S55) for different spin conditions to extract the parameters δ_f and γ_f , see Fig. S3 below.

We use the estimated bandwidth γ_f to calculate the cavity length as $L_f \approx c/(2\gamma_f\mathcal{F})$. For the case of Fig. 3(d) of the main text, the fit (Fig. S3, left panel) yields $\gamma_f/2\pi = 11.5$ kHz, $\delta_f/2\pi = 4.7$ kHz corresponding to $L_f \approx 5$ m. For the spin system with virtual rigidity shown in Fig. 3(f) of the main text, the filter cavity with equivalent performance requires $\gamma_f/2\pi = 8.1$ kHz and $\delta_f/2\pi = 2.7$ kHz resulting in the length $L_f \approx 10$ m, as illustrated with the fit in the right panel of Fig. S3. These values closely match the extrapolated effective Larmor frequency $|\Omega_a^{\text{eff}}|/2\pi = 7.9$ kHz and half effective readout rate $\Gamma_a^{\text{eff}}/4\pi = 2.8$ kHz.

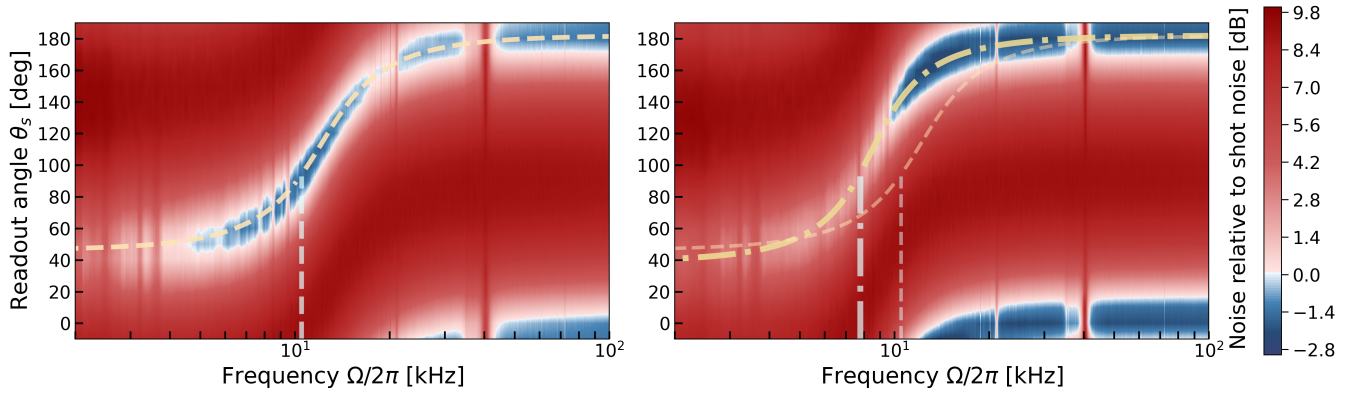


Figure S3. Comparison of the frequency-dependent squeezing generated by our spin system and the model for an analogous filter cavity, Eq. (S55). See explanations in the text.

-
- [1] Zeuthen, E., Polzik, E. S. & Khalili, F. Y. Gravitational wave detection beyond the standard quantum limit using a negative-mass spin system and virtual rigidity. *Phys. Rev. D* **100**, 062004 (2019). URL <https://link.aps.org/doi/10.1103/PhysRevD.100.062004>.
 - [2] Thomas, R. A. *et al.* Entanglement between distant macroscopic mechanical and spin systems. *Nature Physics* **17**, 228–233 (2021). URL <http://dx.doi.org/10.1038/s41567-020-1031-5>.
 - [3] Jia, J. *et al.* Acoustic frequency atomic spin oscillator in the quantum regime. *Nature Communications* **14** (2023). URL <http://dx.doi.org/10.1038/s41467-023-42059-y>.
 - [4] Julsgaard, B., Sherson, J., Sørensen, J. & Polzik, E. S. Characterizing the spin state of an atomic ensemble using the magneto-optical resonancemethod. *Journal of Optics B: Quantum and Semiclassical Optics* **6**, 5 (2003).
 - [5] Ma, Y. *et al.* Proposal for gravitational-wave detection beyond the standard quantum limit through EPR entanglement. *Nature Physics* **13**, 776–780 (2017). URL <http://dx.doi.org/10.1038/nphys4118>.
 - [6] Danilishin, S. L., Khalili, F. Y. & Miao, H. Advanced quantum techniques for future gravitational-wave detectors. *Living Reviews in Relativity* **22** (2019). URL <http://dx.doi.org/10.1007/s41114-019-0018-y>.
 - [7] Gould, D. W. *et al.* Optimal quantum noise cancellation with an entangled witness channel. *Physical Review Research* **3**, 043079 (2021).
 - [8] Wiczeorek, W. *et al.* Optimal state estimation for cavity optomechanical systems. *Physical review letters* **114**, 223601 (2015).
 - [9] Rossi, M., Mason, D., Chen, J. & Schliesser, A. Observing and verifying the quantum trajectory of a mechanical resonator. *Physical review letters* **123**, 163601 (2019).
 - [10] Meng, C. *et al.* Measurement-based preparation of multimode mechanical states. *Science Advances* **8**, eabm7585 (2022).
 - [11] Evans, M., Barsotti, L., Kwee, P., Harms, J. & Miao, H. Realistic filter cavities for advanced gravitational wave detectors. *Physical Review D—Particles, Fields, Gravitation, and Cosmology* **88**, 022002 (2013).

- [12] Kwee, P., Miller, J., Isogai, T., Barsotti, L. & Evans, M. Decoherence and degradation of squeezed states in quantum filter cavities. *Physical Review D* **90**, 062006 (2014).
- [13] McCuller, L. *et al.* Frequency-Dependent Squeezing for Advanced LIGO. *Phys. Rev. Lett.* **124**, 171102 (2020). URL <https://link.aps.org/doi/10.1103/PhysRevLett.124.171102>.
- [14] Ganapathy, D. *et al.* Broadband Quantum Enhancement of the LIGO Detectors with Frequency-Dependent Squeezing. *Phys. Rev. X* **13**, 041021 (2023). URL <https://link.aps.org/doi/10.1103/PhysRevX.13.041021>.